Geophysical Journal International

Geophys. J. Int. (2014) **196,** 317–339
Advance Access publication 2013 November 20

doi: 10.1093/gji/ggt187

Processing of translational and rotational motions of surface waves: performance analysis and applications to single sensor and to array measurements

Stefano Maranò and Donat Fäh

ETH Zurich, Swiss Seismological Service, 8092 *Zürich, Switzerland. E-mail: stefano.marano@sed.ethz.ch*

Accepted 2013 May 7. Received 2013 April 3; in original form 2012 December 17

SUMMARY

The analysis of rotational seismic motions has received considerable attention in the last years. Recent advances in sensor technologies allow us to measure directly the rotational components of the seismic wavefield. Today this is achieved with improved accuracy and at an affordable cost. The analysis and the study of rotational motions are, to a certain extent, less developed than other aspects of seismology due to the historical lack of instrumental observations. This is due to both the technical challenges involved in measuring rotational motions and to the widespread belief that rotational motions are insignificant.

This paper addresses the joint processing of translational and rotational motions from both the theoretical and the practical perspectives. Our attention focuses on the analysis of motions of both Rayleigh waves and Love waves from recordings of single sensors and from an array of sensors. From the theoretical standpoint, analysis of Fisher information (FI) allows us to understand how the different measurement types contribute to the estimation of quantities of geophysical interest. In addition, we show how rotational measurements resolve ambiguity on parameter estimation in the single sensor setting. We quantify the achievable estimation accuracy by means of Cramér–Rao bound (CRB). From the practical standpoint, a method for the joint processing of rotational and translational recordings to perform maximum likelihood (ML) estimation is presented. The proposed technique estimates parameters of Love waves and Rayleigh waves from single sensor or array recordings. We support and illustrate our findings with a comprehensive collection of numerical examples. Applications to real recordings are also shown.

Key words: Time-series analysis; Probability distributions; Surface waves and free oscillations.

1 INTRODUCTION

The joint analysis of translational and rotational motions has the potential to improve the estimation of important physical properties of the near-subsurface. The most striking feature of rotational motions is that, together with translational motions, they enable us to estimate velocity of propagation of seismic waves from a point measurement. The amount of rotational motion induced by a seismic wave is inversely proportional to the wavelength, and is thus related to the velocity of propagation. As a result, a six-components measurement of both translational and rotational motions at a single spatial location gathers sufficient information to estimate the velocity of propagation of a seismic wave. This fact unleashes a myriad of potential applications (Lee *et al.* 2009; Igel *et al.* 2012).

Different approaches to estimate or directly measure rotational motions have been developed in the past decades. In some early applications, ground rotations have been estimated from the spatial derivatives of the translational measurements from an array of sensors (Niazi 1986; Oliveira & Bolt 1989; Spudich *et al.* 1995). In Nigbor (1994), one of the earliest direct measurement of rotational motions, employing a solid-state rotational velocity sensor, is found. Recent advances in sensor technology allow us to directly measure rotational motions with unprecedented accuracy and/or portability (Nigbor *et al.* 2009; Schreiber *et al.* 2009; Lee *et al.* 2012). A technology used in modern and portable rotational sensors relies on an electrochemical transducer where the motion of a fluid caused by an external acceleration is converted into an electrical signal (Leugoud & Kharlamov 2012). A comparison of array derived rotational motions with direct measurements is found in Suryanto *et al.* (2006).

The direct measurement of rotational motions provides an additional independent observation of the seismic wavefield. This is extremely valuable, for instance, in the analysis of surface waves. The measurements of rotational motions supplements the measurements of translational motions, potentially increasing the accuracy of the estimation of the geophysical parameters of interest. Applications relying on the analysis of surface waves are numerous. Notably, the analysis of the seismic wavefield enables us to gather knowledge of geological and geophysical features of the subsoil. Indeed seismic wave attributes such as velocity of propagation or polarization reflect the properties of the structure in which the wave is propagating. The analysis of these properties allow geophysicists to gain insight into the subsoil and the assessment of local seismic hazard relating to the near-surface (Okada 1997; Tokimatsu 1997).

The analysis of recordings from a single sensor is of great practical interest, for example, in engineering seismology. The estimation of seismic parameters from a single sensor is particularly desirable because of the simplicity of measurement operations. Concerning the analysis of translational motions, a well-established single station method is the H/V ratio technique which has been widely used for different purposes (Fäh *et al.* 2003; Bonnefoy-Claudet *et al.* 2006). Other methods estimate Rayleigh wave ellipticity from a single station (Hobiger *et al.* 2009; Poggi *et al.* 2012). The processing of both translational and rotational motions from a single sensor location has been also addressed and it has been shown that the retrieval of wave velocity is possible (Igel *et al.* 2005; Ferreira & Igel 2009).

When plane wavefronts can be assumed, array processing techniques are usually employed. The use of array processing techniques in seismology has a long history. The earliest techniques analysed a single component (Capon 1969; Lacoss *et al.* 1969). More recent developments allow us to separate Love waves and Rayleigh waves (Fäh *et al.* 2008), to estimate Rayleigh wave ellipticity (Poggi & Fäh 2010), and a maximum likelihood (ML) estimation technique also accounting for the presence of multiple waves types (Maranò *et al.* 2012). To the best of our knowledge, at this time there are no applications to seismology of the joint processing of rotational and translational motions for an array of sensors.

In this paper, we are interested in the joint analysis of translational and rotational motions induced by surface waves. We consider different aspects of the problem from a signal processing perspective. We investigate the potential and the limitations introduced through joint processing of these two types of measurement. A method exploiting all the available measurements is presented. Examples are provided to support the theoretical investigation and to show the applicability of the proposed method.

One contribution of this paper is a method for the joint processing of translational motion and rotational motion recordings of surface waves. All the measurements are considered in a single framework and the algorithm provide an ML estimate of the wavefield parameters. We extend a method proposed by the authors in Maranò *et al.* (2012). The original method jointly accounts for the measurement from three components translational sensors and the wavefield parameters of Love waves and Rayleigh waves. The simultaneous presence of multiple waves is also accounted for.

The other main contributions of this paper are the following:

(i) We derive expressions of the Fisher information matrix (FIM) of each statistical model of interest. Fisher information (FI) enables us to gain insight about the contribution of each measurement to the estimation of different wave parameters of interest.

(ii) We show under which conditions, such as number of sensors, type of sensors and wave type, it is possible to identify wave parameters.

(iii) We derive lower bounds on the achievable accuracy of the estimators for the geophysical parameters of interest, namely wavenumber and ellipticity angle. This allows us to compare the performance of any algorithm with an accuracy bound independent of estimation technique and algorithm implementation.

(iv) We provide a comprehensive collection of numerical examples illustrating the potential and limitations of the joint processing of translational and rotational motions.

(v) We show applications of the presented algorithm to two distinct real data sets of the retrieval of Love wavenumber, Rayleigh wavenumber and Rayleigh ellipticity angle for both single sensor and array measurements.

The remainder of the paper is organized as follows. Section 2 presents the system model. The notation used in this manuscript is introduced and Love wave and Rayleigh wave equations for translational and rotational motions are provided. In Section 3, we analyse from a theoretical standpoint the limitations and the performance improvement achievable by including the rotational motions in the processing. In Section 4, we present the algorithm used in this work for the estimation of wavefield parameters. Finally, several numerical results are provided in Section 5, including examples on synthetic data and real applications on two data sets. Conclusions are drawn in Section 6.

2 SYSTEM MODEL

In this paper, we are interested in modelling the seismic wavefield both in its translational motions and its rotational motions. In this section, we introduce wave equations describing quantities of interest and a model of the measurements.

We describe the seismic wavefield, at position $\boldsymbol{p} \in \mathbb{R}^3$ and time t with the vector field $\boldsymbol{u}(\boldsymbol{p}, t) : \mathbb{R}^4 \rightarrow \mathbb{R}^6$

$$\boldsymbol{u}(\boldsymbol{p}, t) = \left(u_x, u_y, u_z, \omega_x, \omega_y, \omega_z\right)(\boldsymbol{p}, t)\,, \tag{1}$$

where the first three components of the vector field describe the translational motions and the last three the rotational motions. For the sake of simplicity, we portray wave equations of the seismic wavefield in displacements and rotations despite the actual measurements may be velocities or accelerations.

We use a 3-D, right-handed Cartesian coordinate system with the z-axis pointing upwards. The azimuth ψ is measured counter-clockwise from the x-axis. The sign of the rotations follows the right-hand rule.

2.1 Rotational motions at a free surface

We now provide the derivation of rotational motions at the free surface. In this section, we omit the dependence on $(\boldsymbol{p}, t)$ for conciseness of notation. From mechanics (Aki & Richards 2002), rotational motions $(\omega_x, \omega_y, \omega_z)$ are related to the curl of translational motions (u_x, u_y, u_z) as

$$(\omega_x, \omega_y, \omega_z) = \frac{1}{2}\nabla \times (u_x, u_y, u_z)$$

$$= \begin{vmatrix} \hat{\boldsymbol{x}} & \hat{\boldsymbol{y}} & \hat{\boldsymbol{z}} \\ \frac{\partial}{\partial x} & \frac{\partial}{\partial y} & \frac{\partial}{\partial z} \\ u_x & u_y & u_z \end{vmatrix}, \tag{2}$$

where $\hat{\boldsymbol{x}}$, $\hat{\boldsymbol{y}}$, $\hat{\boldsymbol{z}}$ are the versors of the coordinate system and where $|\cdot|$ denotes the determinant of the matrix. It follows directly from (2) that

$$\omega_x = \frac{1}{2}\left(\frac{\partial u_z}{\partial y} - \frac{\partial u_y}{\partial z}\right)$$

$$\omega_y = \frac{1}{2}\left(\frac{\partial u_x}{\partial z} - \frac{\partial u_z}{\partial x}\right)$$

$$\omega_z = \frac{1}{2}\left(\frac{\partial u_y}{\partial x} - \frac{\partial u_x}{\partial y}\right). \tag{3}$$

Boundary conditions at the free surface require all the stress along z to vanish and leave the displacement unconstrained. Let $\mathbf{T}$ denote the Cauchy stress tensor, we enforce the boundary conditions as $\mathbf{T}\hat{\boldsymbol{z}} = (0, 0, 0)$. Using Hooke's law for a linear elastic medium, at $z = 0$ the following conditions are found

$$\tau_{x,z} = \mu\left(\frac{\partial u_z}{\partial x} - \frac{\partial u_x}{\partial z}\right) = 0$$

$$\tau_{y,z} = \mu\left(\frac{\partial u_z}{\partial y} - \frac{\partial u_y}{\partial z}\right) = 0$$

$$\tau_{z,z} = \lambda\left(\frac{\partial u_x}{\partial x} + \frac{\partial u_y}{\partial y} + \frac{\partial u_z}{\partial z}\right) + \mu\left(\frac{\partial u_z}{\partial z} - \frac{\partial u_z}{\partial z}\right) = 0\,, \tag{4}$$

where λ and μ are the Lamé parameters. Comparing (3) with (4), it is apparent that the conditions $\tau_{x,z} = 0$ and $\tau_{y,z} = 0$ are influencing the rotational motions. From (4) it is found that

$$\frac{\partial u_z}{\partial x} = \frac{\partial u_x}{\partial z} \qquad \text{and} \qquad \frac{\partial u_z}{\partial y} = \frac{\partial u_y}{\partial z}\,, \tag{5}$$

substituting into (3) we find the rotational motions at the free surface to be

$$\omega_x(\boldsymbol{p}, t) = \frac{\partial u_z(\boldsymbol{p}, t)}{\partial y}$$

$$\omega_y(\boldsymbol{p}, t) = -\frac{\partial u_z(\boldsymbol{p}, t)}{\partial x}$$

$$\omega_z(\boldsymbol{p}, t) = \frac{1}{2}\left(\frac{\partial u_y(\boldsymbol{p}, t)}{\partial x} - \frac{\partial u_x(\boldsymbol{p}, t)}{\partial y}\right). \tag{6}$$

2.2 Translational and rotational motions for surface waves

In this paper, we study waves propagating near the surface of the Earth and having a direction of propagation lying on the horizontal plane $z = 0$. The wave equations we describe hereafter are valid for $z = 0$ and for plane wave fronts. The direction of propagation of a wave is given by the wave vector $\boldsymbol{\kappa} = \kappa\,(\cos\psi, \sin\psi, 0)^{\mathrm{T}}$, whose magnitude κ is the wavenumber.

Love waves exhibit a translational particle motion confined to the horizontal plane, the particle oscillates perpendicular to the direction of propagation. The particle displacement generated by a single monochromatic Love wave at position and time $(\boldsymbol{p}, t)$ is

$$u_x(\boldsymbol{p}, t) = -\alpha \sin\psi \cos(\omega t - \boldsymbol{\kappa} \cdot \boldsymbol{p} + \varphi)$$

$$u_y(\boldsymbol{p}, t) = \alpha \cos\psi \cos(\omega t - \boldsymbol{\kappa} \cdot \boldsymbol{p} + \varphi)$$

$$u_z(\boldsymbol{p}, t) = 0\,, \tag{7}$$

where $\alpha \in \mathbb{R}_+$ and φ denote the amplitude and the phase of the wave, respectively. The temporal angular frequency is denoted with ω. The azimuth ψ indicates the direction of propagation of the wave.

From (7), using (6) the rotational motions induced by a Love wave are found to be

$$\omega_x(\boldsymbol{p}, t) = 0$$

$$\omega_y(\boldsymbol{p}, t) = 0$$

$$\omega_z(\boldsymbol{p}, t) = \frac{1}{2}\alpha\kappa \sin(\omega t - \boldsymbol{\kappa} \cdot \boldsymbol{p} + \varphi)\,. \tag{8}$$

Rotational motions induced by a single Love wave are limited to the ω_z component. Rotations are scaled of a factor $\kappa/2$ with respect to the wave amplitude α.

We define the wavefield parameter vector for a Love wave as $\boldsymbol{\theta}^{(\mathrm{L})} = (\alpha, \varphi, \kappa, \psi)^{\mathrm{T}}$.

Rayleigh waves exhibit a translational particle motion having an elliptical pattern and confined to the vertical plane perpendicular to the surface of the Earth and containing the direction of propagation of the wave. The particle displacement generated by a single Rayleigh wave is

$$u_x(\boldsymbol{p}, t) = \alpha \sin\xi \cos\psi \cos(\omega t - \boldsymbol{\kappa} \cdot \boldsymbol{p} + \varphi)$$

$$u_y(\boldsymbol{p}, t) = \alpha \sin\xi \sin\psi \cos(\omega t - \boldsymbol{\kappa} \cdot \boldsymbol{p} + \varphi)$$

$$u_z(\boldsymbol{p}, t) = \alpha \cos\xi \cos(\omega t - \boldsymbol{\kappa} \cdot \boldsymbol{p} + \pi/2 + \varphi)\,. \tag{9}$$

The angle ξ is called *ellipticity angle* of the Rayleigh wave and determines the eccentricity and the sense of rotation of the particle motion. If $\xi \in (-\pi/2, 0)$, the Rayleigh wave elliptical motion is said to be *retrograde* (i.e. the oscillation on the vertical component (u_z) is shifted by $+\pi/2$ radians with respect to the oscillation on the direction of propagation). If $\xi \in (0, \pi/2)$ the wave is said to be *prograde*. For $\xi = 0$ and $\xi = \pm\pi/2$, the polarization is vertical and horizontal, respectively. The quantity $|\tan\xi|$ is known as the *ellipticity* of the Rayleigh wave. See Maranò *et al.* (2012) for a detailed description of this parametrization.

From (9), using (6) the rotational motions for a Rayleigh wave are found to be

$$\omega_x(\boldsymbol{p}, t) = \alpha\kappa \sin\psi \cos\xi \cos(\omega t - \boldsymbol{\kappa} \cdot \boldsymbol{p} + \varphi)$$

$$\omega_y(\boldsymbol{p}, t) = -\alpha\kappa \cos\psi \cos\xi \cos(\omega t - \boldsymbol{\kappa} \cdot \boldsymbol{p} + \varphi)$$

$$\omega_z(\boldsymbol{p}, t) = 0\,. \tag{10}$$

Rotational motions induced by a single Rayleigh wave are limited to the ω_x and ω_y components. When a Rayleigh wave is horizontally polarized (i.e. $\xi = \pm\pi/2$), no rotational motions are generated.

We define the wavefield parameter vector for a Rayleigh wave as $\boldsymbol{\theta}^{(\mathrm{R})} = (\alpha, \varphi, \kappa, \psi, \xi)^{\mathrm{T}}$.

2.3 Measurement model

The seismic wavefield is sampled at different spatial locations and time instants by means of instrumentation able to measure the translational motions and the rotational motions. At each location a sensor measures the ground translation along the direction of the axes of the coordinate system x, y, z and the ground rotation around the same axes. We say that each sensor has six components.

To measure seismic waves, we deploy an array of N_{s} sensors on the surface of the Earth positioned at locations $\{\boldsymbol{p}_n\}_{n=1,\ldots,N_{\mathrm{s}}}$. We restrict our interest to small aperture arrays and work with a flat Earth model. Each signal is sampled at K instants $\{t_k\}_{k=1,\ldots,K}$. The recording from the six components of the nth sensor are grouped in six channels numbered from $\ell = 6n-5$ to $\ell+5 = 6n$ and ordered as $u_k^{(6n-5)} = u_x(\boldsymbol{p}_n, t_k)$, $u_k^{(6n-4)} = u_y(\boldsymbol{p}_n, t_k)$, $u_k^{(6n-3)} = u_z(\boldsymbol{p}_n, t_k)$, $u_k^{(6n-2)} = \omega_x(\boldsymbol{p}_n, t_k)$, $u_k^{(6n-1)} = \omega_y(\boldsymbol{p}_n, t_k)$ and $u_k^{(6n)} = \omega_z(\boldsymbol{p}_n, t_k)$. We let $L = 6N_{\mathrm{s}}$ denote the total number of channels in an array of six components sensors.

Each measurement is corrupted by independent additive Gaussian noise $Z_k^{(\ell)} \sim \mathcal{N}(0, \sigma_\ell^2)$. Noise variance is, in general, different on each channel

$$Y_k^{(\ell)} = u_k^{(\ell)}(\boldsymbol{\theta}) + Z_k^{(\ell)}\,. \tag{11}$$

The quantities $u_k^{(\ell)}(\boldsymbol{\theta})$ are deterministic functions of wavefield parameters $\boldsymbol{\theta}$ as described in (7)–(10).

It follows from the signal and measurement wave model that the probability density function (PDF) of the measurements is

$$p_{\boldsymbol{Y}}(\boldsymbol{y}|\boldsymbol{\theta}) = \prod_{\ell=1}^{L}\prod_{k=1}^{K} \frac{1}{\sqrt{2\pi\sigma_\ell^2}} \exp\left(-\frac{\left(u_k^{(\ell)}(\boldsymbol{\theta}) - y_k^{(\ell)}\right)^2}{2\sigma_\ell^2}\right), \tag{12}$$

where we grouped the measurements as $\boldsymbol{Y} = \{Y_k^{(\ell)}\}_{\substack{\ell=1,\ldots,L \\ k=1,\ldots,K}}$.

Whenever a sensor has less than six components, the corresponding missing channels are omitted from the product in (12).

AN EXAMPLE OF THE ESTIMATION OF A SINUSOID IN NOISE

We review the statistical tools used in this paper considering a simple toy example. The estimation of amplitude and phase of a sinusoid from noisy measurements is considered. For a comprehensive introduction to estimation theory, we refer the interested reader to Kay (1993).

System model. We consider a sinusoid with known angular frequency ω. The sinusoid is a deterministic function of amplitude α and phase φ, which are unknown. Noisy measurement of the sinusoid are taken at K known time instants $\{t_k\}_{k=1,\dots,K}$. Each measurement Y_k is corrupted by independent additive noise Z_k as

$$Y_k = \alpha \cos(\omega t_k + \varphi) + Z_k \,,$$

for $k = 1, \dots, K$. We assume the statistical properties of the noise to be known. Specifically, the noise has Gaussian distribution with zero mean and known variance σ^2, i.e. $Z_k \sim \mathcal{N}(0, \sigma^2)$.

Probability density function. Given the assumption of independent and identically distributed noise, it is straightforward to write the probability density function (PDF) of the measurements as

$$p_Y(\boldsymbol{y}|\boldsymbol{\theta}) = \prod_{k=1}^{K} \frac{1}{\sqrt{2\pi\sigma^2}} \exp\left(-\frac{(\alpha\cos(\omega t_k + \varphi) - y_k)^2}{2\sigma^2}\right) .$$

The parameter vector $\boldsymbol{\theta} = (\alpha, \varphi)$ collects the parameters of the model that are unknown and need to be estimated.

Likelihood function. Given the measurements $\tilde{\boldsymbol{y}} = \{\tilde{y}_k\}_{k=1,\dots,K}$, the likelihood function (LF) of the observations is $p_Y(\tilde{\boldsymbol{y}}|\boldsymbol{\theta})$. Observe that the LF is a function of $\boldsymbol{\theta}$ and the measurements $\tilde{\boldsymbol{y}}$ are fixed. Given the observations $\tilde{\boldsymbol{y}}$, the LF quantifies how likely are the parameters $\boldsymbol{\theta}$.

Maximum likelihood estimation. To obtain an estimate $\hat{\boldsymbol{\theta}}$ of the true unknown parameters, we choose to follow the maximum likelihood (ML) principle. In this view, it is necessary to find the vector $\boldsymbol{\theta}$ that maximizes the LF

$$\hat{\boldsymbol{\theta}} = \underset{\boldsymbol{\theta}}{\operatorname{argmax}}\, p_Y(\tilde{\boldsymbol{y}}|\boldsymbol{\theta}) \,.$$

Such maximization can often be addressed numerically. However, faster and more accurate analytical solutions may be available.

At least two properties are desirable for an estimator. First, the estimator is often desired to be unbiased. On the average we expect the estimator to provide the true value, i.e. $\mathsf{E}\{\hat{\theta} - \theta\} = 0$, where $\mathsf{E}\{\cdot\}$ denotes the expected value. Second, the estimator should be accurate. Or, in other words, the estimator variance $\mathsf{E}\{(\hat{\theta} - \theta)^2\}$ should be as small as possible. Under certain assumptions, ML estimators are unbiased and have smaller variance that any other unbiased estimator.

Fisher information. Fisher information (FI) quantifies the information we obtain about each parameter from our experiment. The Fisher information matrix (FIM) is defined as

$$\mathcal{I}(\boldsymbol{\theta}) = \mathsf{E}\left\{-\frac{\partial^2 \ln p_Y(\boldsymbol{y}|\boldsymbol{\theta})}{\partial \boldsymbol{\theta}^2}\right\} ,$$

which can be interpreted as the average Hessian matrix at the point $\boldsymbol{\theta}$ of the negative log-likelihood function (LLF). The operator $\mathsf{E}\{\cdot\}$ denotes the expectation over $\boldsymbol{Y}$. Observe that the FIM depends on the statistical model and on the parameter vector $\boldsymbol{\theta}$ but is independent of the measurements.

For our model, the FIM is

$$\mathcal{I}(\boldsymbol{\theta}) = \frac{K}{2\sigma^2}\begin{pmatrix} 1 & 0 \\ 0 & \alpha^2 \end{pmatrix}.$$

Each element on the main diagonal represent the amount of information related to each element of the parameter vector. From the first element, we understand that the FI about the sinusoid amplitude α is proportional to the number of samples K and inversely proportional to the noise power σ^2. From the second element, we understand that the FI about the sinusoid phase φ is related to the number of samples and the noise power in the same way. In addition, the FI about the sinusoid phase increase with the amplitude of the sinusoid itself.

AN EXAMPLE OF THE ESTIMATION OF A SINUSOID IN NOISE (*continued*)

Identifiability. An important sanity check is whether the statistical model considered is identifiable. Loosely speaking, a model is identifiable when the estimation problem is well-posed.

Following our example, consider modelling the noisy measurement of the sinusoid with an alternative statistical model as

$$p_Y(\boldsymbol{y}|\boldsymbol{\theta}') = \prod_{k=1}^{K} \frac{1}{\sqrt{2\pi\sigma^2}} \exp\left(-\frac{(\alpha\cos(\omega t_k + \varphi_1 + \varphi_2) - y_k)^2}{2\sigma^2}\right),$$

where the parameter vector is $\boldsymbol{\theta}' = (\alpha, \varphi_1, \varphi_2)$. It is evident that there is some ambiguity in this parametrization since there are infinite φ_1, φ_2 pairs defining the same sinusoid. Therefore two distinct parameter vectors defining the same PDF exist and thus the model is not identifiable.

When such ambiguity is not immediately evident, another way to verify whether a model is identifiable or not, is to test the singularity of the FIM. For this latter model, is found

$$\mathcal{I}(\boldsymbol{\theta}') = \frac{K}{2\sigma^2}\begin{pmatrix} 1 & 0 & 0 \\ 0 & \alpha^2 & \alpha^2 \\ 0 & \alpha^2 & \alpha^2 \end{pmatrix},$$

which is a singular matrix, as expected for an unidentifiable model.

Cramér–Rao bound. The accuracy of any unbiased estimator is limited by the Cramér-Rao bound (CRB). In other words, for a given statistical model there is no unbiased estimator having variance smaller than the CRB. In practice, the CRB is obtained from the elements on the main diagonal of the matrix inverse of $\mathcal{I}(\boldsymbol{\theta})$.

In our example, the computation of $\mathcal{I}^{-1}(\boldsymbol{\theta})$ is straightforward since the matrix $\mathcal{I}(\boldsymbol{\theta})$ is diagonal. From the elements on the main diagonal of $\mathcal{I}^{-1}(\boldsymbol{\theta})$, it is found that the variance of amplitude and phase estimates are lower bounded as

$$\mathsf{E}\left\{(\hat{\alpha} - \mathsf{E}\{\hat{\alpha}\})^2\right\} \geq \frac{2\sigma^2}{K},$$

$$\mathsf{E}\left\{(\hat{\varphi} - \mathsf{E}\{\hat{\varphi}\})^2\right\} \geq \frac{2\sigma^2}{\alpha^2 K}.$$

This analytic result provides insights useful for the design of the experiment and a benchmark that allows to evaluate the performance of an estimation algorithm.

3 THEORETICAL PERFORMANCE ANALYSIS

In this section, we discuss the advantages and potential of the joint processing of rotational and translational measurements from a theoretical standpoint. To this aim, we use several ideas from estimation theory. A reader unfamiliar with this branch of statistics may refer to the box 'An example of the estimation of a sinusoid in noise' included in this paper.

First, we derive an expression of the Fisher information matrix (FIM) for each wave model considered. Then we look at the issue of the identifiability of statistical models concerning Love wave and Rayleigh wave for three components (translational) single sensor, six components (translational and rotational) single sensors, and arrays of sensors. Following, we find the smallest achievable mean-square estimation error (MSEE) of an unbiased estimator using the Cramér-Rao bound (CRB). The contribution to the parameter estimation of the different measurements and parameters is also understood. At last, we briefly discuss the estimator performance at lower signal-to-noise ratio (SNR), in the threshold region.

3.1 Introduction

The MSEE of an estimation algorithm can be computed numerically using Monte Carlo methods. For example, it is sufficient to repeat a large number of times the estimation of the wavefield parameters of a known wave with different noise realizations to compute the MSEE. In this way, it is possible to quantitatively compare the estimation accuracy of two different estimation algorithms or the estimation accuracy of the same estimation algorithm under different conditions. The CRB, provides a lower bound on estimator variance and is independent of estimation technique and algorithm implementation. Therefore, the MSEE of any algorithm can be compared with the CRB. Fig. 1 illustrates these concepts with an example.

It is known from literature that non-linear estimators exhibit an abrupt increase in the MSEE below a certain SNR or sample size. This behaviour is called *threshold effect* and is due to a transition from local to global estimation errors (Van Trees 2001). Three operation regions

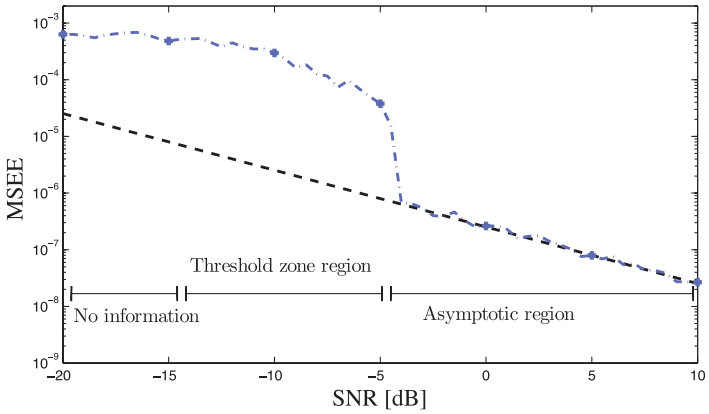

Figure 1. An example of the MSEE of a ML estimator. The MSEE is depicted with a blue dashed line. In the no information region, the MSEE is very large and constrained by the implementation of the algorithm. In the threshold region the occurrence of outliers keep the MSEE significantly larger than the CRB. At last, in the asymptotic region, the MSEE is well described by the CRB, which is shown with the black dashed line.

for the estimator are defined at different SNR ranges, see also Fig. 1. At very low SNR, the noise dominates over the signal of interest, this is called *no information* region. At larger SNR, is found the *threshold region*. The MSEE is still considerably large as global estimation errors occur. Global estimation are also known as outliers. At even larger SNR is found the *asymptotic region.* Local estimation error occurs in this region and the MSEE of a ML estimator is well described by the CRB.

Preliminary definitions:

Consider the following definitions related to the geometrical layout of the array. We introduce the coordinate system (a, b), which is related to (x, y) as

$$\begin{pmatrix} a \\ b \end{pmatrix} = \begin{pmatrix} \cos\psi & \sin\psi \\ -\sin\psi & \cos\psi \end{pmatrix} \begin{pmatrix} x \\ y \end{pmatrix}, \tag{13}$$

where the angle of rotation is the azimuth ψ. Therefore, a is the axis along the direction of propagation of the wave and b the axis perpendicular to it. In this rotated coordinate system we consider the new sensor positions $\{(a_n, b_n)\}_{n=1,\ldots,N_s}$. The moment of inertia (MOI) of the array in the coordinate system with (a, b) are defined as

$$Q_{aa} = \sum_{n=1}^{N_s} (a_n - \bar{a})^2, \tag{14}$$

$$Q_{bb} = \sum_{n=1}^{N_s} (b_n - \bar{b})^2, \tag{15}$$

$$Q_{ab} = \sum_{n=1}^{N_s} (a_n - \bar{a})(b_n - \bar{b}), \tag{16}$$

where $\bar{a} = \frac{1}{N_s}\sum_{n=1}^{N_s} a_n$ and $\bar{b} = \frac{1}{N_s}\sum_{n=1}^{N_s} b_n$ define the *phase centre* of the array.

We observe that the MOIs are invariant to a translation of the array and that for the single sensor setting ($N_s = 1$) all the MOIs are equal to zero.

3.2 Fisher information

When combining the measurements of translational and rotational motions, one question that arises naturally is how and to which extent the different measurements contribute to the parameter estimation of the statistical model.

The Fisher information (FI) conveys the amount of information about a statistical parameter carried by the PDF of the observations (Fisher 1922). For a statistical model with multiple parameters the FIM is given by

$$\mathcal{I}(\boldsymbol{\theta}) = \mathsf{E}\left\{ -\frac{\partial^2 \ln p_Y(\boldsymbol{y}|\boldsymbol{\theta})}{\partial \boldsymbol{\theta}^2} \right\}, \tag{17}$$

where $\mathsf{E}\{\cdot\}$ denotes the expectation operation. The vector $\boldsymbol{\theta}$ collects the unknown wavefield parameters of either Love wave or Rayleigh wave. The matrix $\mathcal{I}$ is a square symmetric matrix with as many columns as the elements in the vector $\boldsymbol{\theta}$.

Measurements of translational and rotational motions are independent corrupted by additive white Gaussian noise, as in (11). Throughout this section we consider the translational and the rotational components to be subject to different noise levels, with power σ_{t}^2 and σ_{r}^2, respectively.

For independent observations, the FIM is additive. Let $\mathcal{I}_{\mathrm{t}}(\boldsymbol{\theta})$ and $\mathcal{I}_{\mathrm{r}}(\boldsymbol{\theta})$ be the FIM pertaining the translational and the rotational components. The FIM accounting for all the observations is obtained as

$$\mathcal{I}(\boldsymbol{\theta}) = \mathcal{I}_{\mathrm{t}}(\boldsymbol{\theta}) + \mathcal{I}_{\mathrm{r}}(\boldsymbol{\theta})\,. \tag{18}$$

In Appendix A, the expressions of the FIMs, together with an outline of the derivation, are provided. The FIMs for the model of a single Love wave are given in (A5) and in (A6) for translational and rotational measurements, respectively. The FIMs for a single Rayleigh wave are given in (A8) and in (A9) for translational and rotational measurements, respectively.

We observe that the diagonal elements of the FIM correspond to the FI of a certain parameter when all the other parameters are known. In other words, the uncertainty associated with the other unknown parameters is neglected if a single element on the diagonal is considered.

3.3 Identifiability

Consider a statistical model described in terms of its PDF $p_{\boldsymbol{Y}}(\boldsymbol{y}|\boldsymbol{\theta})$ parametrized with a vector $\boldsymbol{\theta} \in \Theta$. A statistical model is said to be *identifiable* when the mapping $\boldsymbol{\theta} \to p_{\boldsymbol{Y}}(\boldsymbol{y}|\boldsymbol{\theta})$ is bijective (Rothenberg 1971)

$$p_{\boldsymbol{Y}}(\boldsymbol{y}|\boldsymbol{\theta}_1) = p_{\boldsymbol{Y}}(\boldsymbol{y}|\boldsymbol{\theta}_2) \Leftrightarrow \boldsymbol{\theta}_1 = \boldsymbol{\theta}_2 \;\; \forall \boldsymbol{\theta}_1, \boldsymbol{\theta}_2 \in \Theta\,. \tag{19}$$

This definition means that two distinct parameter vectors which specify the same statistical model do not exist. Whenever condition (19) does not hold, the model is said to be *unidentifiable*. The analysis in this section is limited to the *local* identifiability, that is, to a neighbourhood of the maximum likelihood point.

In addition, a statistical model is identifiable if and only if the corresponding FIM is non-singular (Rothenberg 1971).

3.3.1 Love wave, single sensor

Consider the problem of estimating wavefield parameters $\boldsymbol{\theta}^{(\mathrm{L})} = (\alpha, \varphi, \kappa, \psi)^{\mathrm{T}}$ for a Love wave from the measurements of a single three-components (translational) sensor. From (7), we understand that this model is not identifiable as several parameters specify the same PDF. Consider, for example, the parameter vectors $\boldsymbol{\theta}_1^{(\mathrm{L})} = (\alpha, \varphi, \kappa, \psi)^{\mathrm{T}}$, $\boldsymbol{\theta}_2^{(\mathrm{L})} = (\alpha, \varphi, \gamma\kappa, \psi)^{\mathrm{T}}$ with $\gamma \in \mathbb{R}_+$ and $\boldsymbol{\theta}_3^{(\mathrm{L})} = (\alpha, \varphi, \kappa, \psi + \pi)^{\mathrm{T}}$, they specify the same distribution, i.e. $p_{\boldsymbol{Y}}(\boldsymbol{y}|\boldsymbol{\theta}_1^{(\mathrm{L})}) = p_{\boldsymbol{Y}}(\boldsymbol{y}|\boldsymbol{\theta}_2^{(\mathrm{L})}) = p_{\boldsymbol{Y}}(\boldsymbol{y}|\boldsymbol{\theta}_3^{(\mathrm{L})})$. Indeed, with a single translational sensor is not possible to determine the wave vector, and thus the velocity of propagation, of the Love wave. Moreover, there is an ambiguity of 180° about the direction of propagation.

The related problem of estimating wavefield parameters $\boldsymbol{\theta}^{(\mathrm{L})}$ for a Love wave from a single six (translational and rotational) sensor is, however, well-posed. From (7) and (8), we understand that this model is identifiable as two distinct parameter vectors $\boldsymbol{\theta}_1^{(\mathrm{L})} \neq \boldsymbol{\theta}_2^{(\mathrm{L})}$ specifying the same distribution do not exist. This fact can be verified by checking the non-singularity of the FIM in (A7) for $N_{\mathrm{s}} = 1$. The same conclusion has been reached using different arguments in Ferreira & Igel (2009) and Fichtner & Igel (2009).

3.3.2 Rayleigh wave, single sensor

We now consider the problem of estimating wavefield parameters $\boldsymbol{\theta}^{(\mathrm{R})} = (\alpha, \varphi, \kappa, \psi, \xi)^{\mathrm{T}}$ for a Rayleigh wave from the measurements of a single three-components (translational) sensor. From (9), we understand that this model is not identifiable as several parameters specify the same distribution. Indeed the parameter vectors $\boldsymbol{\theta}_1^{(\mathrm{R})} = (\alpha, \varphi, \kappa, \psi, \xi)^{\mathrm{T}}$, $\boldsymbol{\theta}_2^{(\mathrm{R})} = (\alpha, \varphi, \gamma\kappa, \psi, \xi)^{\mathrm{T}}$ with $\gamma \in \mathbb{R}_+$ and $\boldsymbol{\theta}_3^{(\mathrm{R})} = (\alpha, \varphi, \kappa, \psi + \pi, -\xi)^{\mathrm{T}}$ specify the same PDF. Again, from a single sensor is not possible to retrieve any information concerning wave velocity of propagation. Moreover, there is an ambiguity involving direction of propagation and the prograde/retrograde sense of rotation.

For a six components sensor the estimation of $\boldsymbol{\theta}^{(\mathrm{R})}$ is well-posed. This can be understood from (9) and (10). Again, this can be verified by checking the non-singularity of the FIM of (A10) for $N_{\mathrm{s}} = 1$.

3.3.3 Array of sensors

It is well known that by means of an array of three components (translational) sensors it is possible to estimate wavefield parameters of either a Love wave or a Rayleigh wave. The only exception is the case of collinear sensors. Indeed a linear array cannot resolve the wavenumber for a wave propagating perpendicular to the array. When employing an array of six components (translational and rotational) the limitation of the linear array is no more present. Both these facts can be verified by testing the singularity of the FIMs.

Interestingly, with an array of three components (rotational) sensors it is possible to identify the parameters of a Love wave but not the parameters of a Rayleigh wave. Indeed an array of sole rotational sensors it is not capable of estimating correctly Rayleigh wave amplitude, phase, and ellipticity. The parameter vectors $\boldsymbol{\theta}_1^{(\mathrm{R})} = (\alpha, \varphi, \kappa, \psi, \xi)$, $\boldsymbol{\theta}_2^{(\mathrm{R})} = (\gamma\alpha, \varphi, \kappa, \psi, \arccos(\cos\xi/\gamma))$ with $\gamma \in \mathbb{R}_+$ and $\boldsymbol{\theta}_3^{(\mathrm{R})} = (\alpha, \varphi + \pi, \kappa, \psi, -\xi)$ specify the same statistical model.

3.4 Cramér-Rao bound

The Cramér-Rao bound (CRB) is a lower bound on the variance of unbiased estimators (Rao 1945; Cramér 1946). Knowledge of a lower bound on the estimator variance has at least two practical implications. First, it allows us to evaluate the performance of an estimation algorithm, by enabling a quantitative comparison between the mean-square estimation error (MSEE) of the algorithm under test and the smallest achievable variance. Second, the analytic expression of the CRB enables us to design the experiment set up in order to reduce the lower bound and therefore increase the amount of information gathered by the experiment.

The information inequality states that the MSEE of an unbiased estimator is lower bounded as

$$\mathsf{E}\left\{\left(\hat{\boldsymbol{\theta}}-\mathsf{E}\{\hat{\boldsymbol{\theta}}\}\right)\left(\hat{\boldsymbol{\theta}}-\mathsf{E}\{\hat{\boldsymbol{\theta}}\}\right)^{\mathrm{T}}\right\}\succeq\left(\boldsymbol{\mathcal{I}}(\boldsymbol{\theta})\right)^{-1}. \tag{20}$$

where $\mathbf{A}\succeq\mathbf{B}$ means that the matrix $\mathbf{A}-\mathbf{B}$ is positive semidefinite (PSD). In particular, we are interested in the diagonal elements of $\boldsymbol{\mathcal{I}}^{-1}$ as they provide a lower bound on the MSEEs of the corresponding parameters.

In high SNR regime, the CRB well describes the performance of ML estimator (*cf.* Fig. 1). Thus in order to increase estimation accuracy, one is interested to reduce the CRB. This can be achieved by tuning the value of some deterministic parameters of the model as, for example, increasing the number of sensors or optimizing the array geometry.

To derive the CRB for the wavefield parameters of interest is necessary to invert the FIM $\boldsymbol{\mathcal{I}}$. The CRB is obtained from the elements on the main diagonal of $\boldsymbol{\mathcal{I}}^{-1}$. Since we are interested in the elements on themain diagonal of $\boldsymbol{\mathcal{I}}^{-1}$ corresponding to wavenumber and ellipticity angle, we avoid the complete inversion of $\boldsymbol{\mathcal{I}}$ as follows. We partition the FIM as

$$\boldsymbol{\mathcal{I}}(\boldsymbol{\theta})=\begin{pmatrix} c & \boldsymbol{d}^{\mathrm{T}} \\ \boldsymbol{d} & \mathbf{G}\end{pmatrix}, \tag{21}$$

where c is a scalar, $\boldsymbol{d}$ is a vector, and $\mathbf{G}$ is a matrix of suitable sizes. The element in the first position of $\boldsymbol{\mathcal{I}}^{-1}$ is then found to be

$$\left[\left(\boldsymbol{\mathcal{I}}(\boldsymbol{\theta})\right)^{-1}\right]_{1,1}=\left(c-\boldsymbol{d}^{\mathrm{T}}\mathbf{G}^{-1}\boldsymbol{d}\right)^{-1}, \tag{22}$$

where $[\cdot]_{i,j}$ denotes the element of the matrix in position (i,j) (Horn & Johnson 1990).

In (22), the quantity $c-\boldsymbol{d}^{\mathrm{T}}\mathbf{G}^{-1}\boldsymbol{d}$ has the dimension of FI and has been referred to by some authors as equivalent Fisher information (EFI) (Shen & Win 2010). In contrast with FI, the EFI accounts for the uncertainty introduced by the other unknown parameters of the statistical model. The term c is exactly the FI of the parameter of interest. The term $\boldsymbol{d}^{\mathrm{T}}\mathbf{G}^{-1}\boldsymbol{d}$ is non-negative since $\mathbf{G}$ is PSD being a diagonal sub-block of a PSD matrix. This last quantity accounts for the uncertainty due to the other parameters.

It is now clear that reducing the CRB is equivalent to increase the EFI. In other words, increasing the EFI is desirable as better estimation accuracy can be achieved.

In order to use (22) effectively, it may be necessary to permute the row and columns of $\boldsymbol{\mathcal{I}}$ such that the element of interest is in the top-left-most position. This can be accomplished using a permutation matrix $\mathbf{P}$ and consider the re-arranged $\boldsymbol{\mathcal{I}}'$ obtained as $\boldsymbol{\mathcal{I}}'=\mathbf{P}^{\mathrm{T}}\boldsymbol{\mathcal{I}}\mathbf{P}$.

In the following, we restrict ourselves to the analysis of the CRB of wavenumber and ellipticity angle as these are the parameters of greater practical interest.

3.4.1 Love wave wavenumber

The CRB on Love wavenumber for translational measurements is obtained using (22) and (A5). The MSEE of Love wave wavenumber is lower bounded as

$$\mathsf{E}\left\{(\hat{\kappa}-\mathsf{E}\{\hat{\kappa}\})^2\right\}\geq\left(\frac{\alpha^2K}{2\sigma_{\mathrm{t}}^2}\left(Q_{aa}-\frac{Q_{ab}^2}{Q_{bb}+N_{\mathrm{s}}/\kappa^2}\right)\right)^{-1}. \tag{23}$$

The CRB is directly proportional to noise power σ_t^2, inversely proportional to the amplitude of the wave α and to the number of samples K. We observe that K cannot be arbitrarily increased as the validity of the model described in (7) may be no longer valid for long observations because of the time variability of real seismic sources. We emphasize that the CRB depends on the sensor positions $\{\boldsymbol{p}_n\}_{n=1,\ldots,N_{\mathrm{s}}}$ only trough the MOIs. The term Q_{aa} is representative of the information contribution due to the spatial sampling of the wavefield. A large Q_{aa} can be obtained with a large aperture array along the direction of wave propagation a, *cf.* (14). However observe that a large aperture may invalidate the plane wave assumption. The last term is due to the uncertainty of the other wavefield parameters and increases the CRB. It can be eliminated by choosing an array geometry such that $Q_{ab}=0$.

The CRB on Love wavenumber for rotational measurements is obtained using (22) and (A6). The MSEE of Love wave wavenumber is lower bounded as

$$\mathsf{E}\left\{(\hat{\kappa}-\mathsf{E}\{\hat{\kappa}\})^2\right\}\geq\left(\frac{\alpha^2\kappa^2K}{8\sigma_{\mathrm{r}}^2}\left(Q_{aa}-\frac{Q_{ab}^2}{Q_{bb}}\right)\right)^{-1}. \tag{24}$$

The CRB is similar to the expression in (23). One difference is the presence of a factor $4/\kappa^2$. This is due to the different overall amplitude of the signal measured on ω_z. Concerning seismic surface waves, the κ is generally a small quantity (smaller than one) thus the CRB is increased. In addition, the smaller the wavenumber, the less information is obtained from this type of measurement.

The CRB on Love wavenumber for joint translational and rotational measurements is obtained using (22) with the FIM for the joint measurements (A7). The MSEE of Love wave wavenumber is lower bounded as

$$\mathsf{E}\left\{(\hat{\kappa}-\mathsf{E}\{\hat{\kappa}\})^2\right\} \geq \left(\left(C_\mathrm{t}+\kappa^2 C_\mathrm{r}/4\right) Q_{aa} + \frac{C_\mathrm{t}C_\mathrm{r}N_\mathrm{s}/4}{C_\mathrm{t}+C_\mathrm{r}\kappa^2/4} - \frac{Q_{ab}^2\left(C_\mathrm{t}+\kappa^2 C_\mathrm{r}/4\right)^2}{C_\mathrm{t}N_\mathrm{s}/\kappa^2+(C_\mathrm{t}+\kappa^2 C_\mathrm{r}/4)}\right)^{-1}, \tag{25}$$

with $C_\mathrm{t}=\alpha^2K/2\sigma_\mathrm{t}^2$ and $C_\mathrm{r}=\alpha^2K/2\sigma_\mathrm{r}^2$. The first and the third addends of the sum are, similarly to (23) and (24), representative of the information contributed by the spatial sampling of the wavefield and the uncertainty due to the other parameters weighted by the quality of the signal on the translational and the rotational components. The second addend is representative of the information gain due to the joint processing of the translational and rotational measurements. This term is proportional to N_s and does not go to zero in the single sensor case, so that a single rotational sensors carries information about the wavenumber.

3.4.2 Rayleigh wave wavenumber

The CRB on Rayleigh wavenumber for translational measurements is obtained using (22) and (A8). The MSEE of Rayleigh wave wavenumber is lower bounded as

$$\mathsf{E}\left\{(\hat{\kappa}-\mathsf{E}\{\hat{\kappa}\})^2\right\} \geq \left(\frac{\alpha^2K}{2\sigma_\mathrm{t}^2}\left(Q_{aa}-\frac{Q_{ab}^2}{Q_{bb}+N_\mathrm{s}\sin^2\xi/\kappa^2}\right)\right)^{-1}. \tag{26}$$

This result is similar to (23) and the same considerations apply.

The CRB on Rayleigh wavenumber for rotational measurements is obtained using (22) and (A9). The MSEE of Rayleigh wave wavenumber is lower bounded as

$$\mathsf{E}\left\{(\hat{\kappa}-\mathsf{E}\{\hat{\kappa}\})^2\right\} \geq \left(\frac{\alpha^2\kappa^2\cos^2(\xi)K}{2\sigma_\mathrm{r}^2}\left(Q_{aa}-\frac{Q_{ab}^2}{Q_{bb}+N_\mathrm{s}/\kappa^2}\right)\right)^{-1}. \tag{27}$$

This result is similar to (24) and the same considerations apply. Observe that when the Rayleigh wave is horizontally polarized ($\xi=\pm\pi/2$) the EFI is zero since no rotations are induced by the Rayleigh wave.

The CRB on Rayleigh wavenumber for joint translational and rotational measurements is obtained using (22) with the FIM for the joint measurements (A10). The MSEE of Rayleigh wave wavenumber is lower bounded as

$$\mathsf{E}\left\{(\hat{\kappa}-\mathsf{E}\{\hat{\kappa}\})^2\right\} \geq \left(\Phi Q_{aa} + \frac{C_\mathrm{t}C_\mathrm{r}N_\mathrm{s}\cos^2\xi}{C_\mathrm{t}+\kappa^2C_\mathrm{r}} - \frac{Q_{ab}^2\Phi^2}{C_\mathrm{t}\sin^2\xi N_\mathrm{s}/\kappa^2 + C_\mathrm{r}\cos^2\xi N_\mathrm{s}+\Phi Q_{bb}}\right)^{-1}, \tag{28}$$

with $\Phi=C_\mathrm{t}+C_\mathrm{r}\kappa^2\cos^2\xi$ and $\Psi=C_\mathrm{t}\sin^2\xi+C_\mathrm{r}\kappa^2\cos^2\xi$. This result is similar to (25) and the same considerations apply. We observe that when the Rayleigh wave is horizontally polarized ($\xi=\pm\pi/2$) then (28) reduces to (26) since no rotations are induced by the Rayleigh wave and thus no information is added by the rotational measurements.

3.4.3 Rayleigh wave ellipticity angle

The CRB on Rayleigh ellipticity angle for translational measurements is obtained using (22) and (A8). The MSEE of Rayleigh wave ellipticity angle is lower bounded as

$$\mathsf{E}\left\{(\hat{\xi}-\mathsf{E}\{\hat{\xi}\})^2\right\} \geq \left(\frac{\alpha^2K}{2\sigma_\mathrm{t}^2}N_\mathrm{s}\right)^{-1}. \tag{29}$$

This quantity is related to the number of sensors and it is not affected by the geometry of the array.

As discussed earlier in this section, an array of sole rotational sensors is not able to estimate Rayleigh wave ellipticity angle as the model is unidentifiable.

The CRB on Rayleigh ellipticity angle for joint translational and rotational measurements is obtained using (22) with the FIM for the joint measurements (A10). The MSEE of Rayleigh wave ellipticity angle is lower bounded as

$$\mathsf{E}\left\{(\hat{\xi}-\mathsf{E}\{\hat{\xi}\})^2\right\} \geq \left(C_\mathrm{t}N_\mathrm{s} + \frac{\kappa^2\Phi\left(Q_{aa}\Psi N_\mathrm{s}-\kappa^2(Q_{ab}^2-Q_{aa}Q_{bb})\Phi\right)}{N_\mathrm{s}C_\mathrm{r}C_\mathrm{t}\cos^2\xi(\Psi N_\mathrm{s}+\kappa^2\Phi Q_{bb})+Q_{aa}\Psi\Phi^2N_\mathrm{s}-\kappa^2(Q_{ab}^2-Q_{aa}Q_{bb})\Phi^3}\right)^{-1}. \tag{30}$$

This latter expression is however not immediate to interpret.

3.5 Threshold zone performance

Benefits of processing jointly multiple components in terms of reduction of global errors are well known in literature (Hawkes & Nehorai 1998; Cox & Lai 2007). Performance in the threshold zone of direction of arrival estimators is studied in detail in Athley (2008). In this work, this issue is not addressed directly, however we emphasize that the use of additional measurements reduces the magnitude of local maxima other than the true maximum of the LF and thus of global errors. Improvement in accuracy are to be expected in the low-SNR regime, that is, threshold zone. Performance in the threshold zone are not easily quantifiable analytically and we limit ourselves in presenting some numerical examples in Sections 5.3 and 5.4.

4 PROCESSING TECHNIQUE

In this work we employ an extension of the method presented in Maranò *et al.* (2012). The method allows us to perform ML estimation of wavefield parameters for Love waves and Rayleigh waves relying on observation from seismic sensors. The method models jointly measurements from all sensor components making optimal use of the available information. The wavefield parameters are also estimated jointly. The noise variance on each channel is estimated adaptively. Information from the different channel is merged according to the different noise levels on the different sensor components.

In our approach, we model the system by means of a probabilistic graphical model. A complex system where a large number of random variables and statistical parameters interact with complex relationships can be effectively represented by a graphical model. Within the graphical model, observed random variables (measurements), unobserved random variables and parameters of the statistical model are represented in a unique framework together with the functional relationships occurring among them. The probabilistic graph can be used to perform inference tasks in an efficient manner. As an example, likelihood of the observations and thus ML estimation can be performed exploiting the structure of the graph. By using the graph it is possible to understand the relationship between the different parts of the stochastic system and then, for example, derive sufficient statistics which enable to efficiently compute statistical quantities of interest. In our approach we rely on factor graphs, one flavour among many graphical modelling techniques (Kschischang *et al.* 2001; Loeliger 2004; Loeliger *et al.* 2007).

Using (12) it is possible to compute the likelihood of the observations $\tilde{\boldsymbol{y}}$ for a specific wavefield parameter vector $\boldsymbol{\theta}$ directly. A maximization over the parameter space allows us to obtain a ML estimate $\hat{\boldsymbol{\theta}}$ as

$$\hat{\boldsymbol{\theta}} = \underset{\boldsymbol{\theta}}{\operatorname{argmax}}\, p_Y(\tilde{\boldsymbol{y}}|\boldsymbol{\theta})\,. \tag{31}$$

In this context, different sensor technologies are used and the amplitudes of the measured signals are expected to vary greatly. It would be surely not optimal to assume equal noise variance on every channel. Thus, after estimating the wavefield parameters the noise variances are also estimated as

$$(\hat{\sigma}_1^2, \ldots, \hat{\sigma}_L^2) = \underset{(\sigma_1^2,\ldots,\sigma_L^2)}{\operatorname{argmax}}\; p_Y(\tilde{\boldsymbol{y}}|\hat{\boldsymbol{\theta}}, \sigma_1^2, \ldots, \sigma_L^2)\,, \tag{32}$$

where $\hat{\boldsymbol{\theta}}$ is the estimated wavefield parameter vector obtained from (31).

The maximizations in (31) and in (32) are repeated alternatively and the estimation of the wavefield parameters accounts for the different noise level on the different sensors. Since the likelihood is a finite value the alternating maximizations are guaranteed to converge.

In our implementation, the maximizations in (31) and in (32) are not computed directly from (12). Details concerning the functioning and the implementation of our algorithm are found in Maranò *et al.* (2012) and references therein. In particular, in Reller *et al.* (2011) and in Maranò *et al.* (2011), we explain in detail the design of the factor graph which allows us to derive a sufficient statistic. This allows to perform ML parameter estimation in a computationally attractive manner.

5 NUMERICAL RESULTS

5.1 Introduction

We provide some details about processing and the presentation of some results. Frequencies are processed independently. Unless differently noted, we apply no preprocessing to the recordings other than mean removal. The whole signal is split in time windows where the signal is assumed to be stationary. The length of such time windows is non-adaptive and not dependent on frequency.

We define the SNR as

$$\mathrm{SNR} = \frac{\alpha^2}{2\sigma_{\mathrm{t}}^2}, \tag{33}$$

where σ_{t}^2 is the noise variance on the translational components.

It is clear from (8) and (10) that rotational motions have significantly smaller amplitude than translational motions. Depending on the value of the wavenumber κ, rotational motions can be even one or two order of magnitude smaller than the translational counterparts.

In the numerical examples that follow, we choose the true value of the variance on the rotational components to be $\sigma_r^2 = \kappa^2\sigma_t^2$. This choice is motivated by the fact that the different noise level allows to obtain measurements of comparable SNR on translational and rotational components. Both in the synthetic examples and in the real data set the noise variances are unknown to the algorithm and are estimated with the proposed algorithm as in (32).

In Sections 5.2 and 5.3 we present numerical examples to illustrate the potential and the benefit introduced by the joint processing of translational and rotational components over the processing of the sole translational components. In Section 5.4, we quantify increased estimation accuracy, in terms of MSEE, achieved by employing the rotational measurements and compare with the CRB. At last in Sections 5.5 and 5.6, we show two applications from translational and rotational recordings of a building demolition and an explosion.

5.2 Example likelihood functions for single sensor

By means of numerical examples, we show how the joint processing of translational components and rotational components enables us to identify statistical models for surface waves and to estimate correctly the wave parameters.

The figures shown in this section and in the following should be seen as explanatory examples. In first place, a different noise realization will lead to a different LF. More importantly, a different choice of σ_t^2 and σ_r^2 could lead to a substantially different shape of the LF. To reduce this effects and to ensure a fair comparison, we use a high SNR (SNR $= 10$ dB) and $\sigma_r^2 = \kappa^2\sigma_t^2$. We consider 1 s of observation, sampling at 100 Hz monochromatic waves of frequency $\omega = 2\pi$. Maxima points of the LFs are marked with white crosses.

In Fig. 2, the LLFs of observations of a noisy Love wave are shown. A single Love wave with $\boldsymbol{\theta}^{(\mathrm{L})} = (1, 0, 0.05, \pi/4)^{\mathrm{T}}$ is considered. Fig. 2(a) depicts the LLF obtained from a single three components (translational) sensor. A whole set of points, namely the line defined by the set $\{(\alpha, \varphi, \kappa, \psi)\colon \alpha = 1, \varphi = 0, \kappa \geq 0, \psi \in \{\pi/4, 5\pi/4\}\}$, maximize the likelihood of the observations. This reflects the inability to determine wavenumber and azimuth from a single three components sensor.

Fig. 2(b) depicts the LLF obtained from a single six components (translational and rotational) sensor. The global maximum point is seen in correspondence of the true wavefield parameters. Indeed a single six components sensor allows the determination of velocity of propagation and direction of propagation without ambiguity.

A similar setup is repeated for a single Rayleigh wave with parameters $\boldsymbol{\theta}^{(\mathrm{R})} = (1, 0, 0.05, \pi/4, -\pi/4)^{\mathrm{T}}$. In Fig. 3, the LLFs of observations of a noisy Rayleigh wave are shown. We are interested in showing the shape of the LLF as a function of three parameters, namely wavenumber, ellipticity and azimuth. Thus, we depict three slices of the LLFs, each slice is a function of two parameters for a fixed value of the third parameter equal to the true value.

Figs 3(a), (c) and (e) depict slices of the LLF obtained from a single three components (translational) sensor. A whole set of points, namely the set $\{(\alpha, \varphi, \kappa, \psi, \xi)\colon \alpha = 1, \varphi = 0, \kappa \geq 0, (\psi = \pi/4, \xi = -\pi/4) \vee (\psi = 5\pi/4, \xi = \pi/4)\}$, maximize the likelihood of the observations. This reflects the inability to determine unambiguously wavenumber, azimuth and sense of rotation of the Rayleigh wave from a single three components sensor.

In contrast, from a single six components (translational and rotational) sensor is possible to estimate wavefield parameters correctly. Figs 3(b), (d) and (f) depict the same slices obtained from a single six components (translational and rotational) sensor. The global maximum

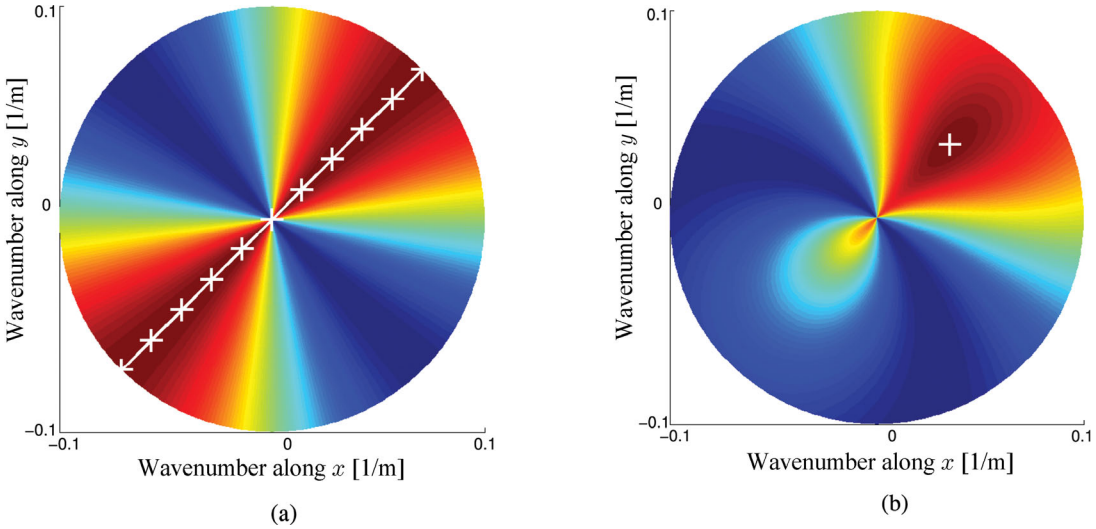

Figure 2. Log-likelihood functions (LLFs) of observations from a single sensor of a single Love wave as a function of wavenumber along x, $\kappa\cos\psi$ and wavenumber along y, $\kappa\sin\psi$. Comparison of analysis of sole translational components (left-hand panel) and joint translational and rotational components (right-hand panel). Large log-likelihood (LL) values are shown with colours towards red and low LL values with colours towards blue. (a) A line across the origin individuate the maxima point of the LLF reflecting the inability to determine velocity of propagation and direction of propagation. (b) The LLF exhibits a single maxima.

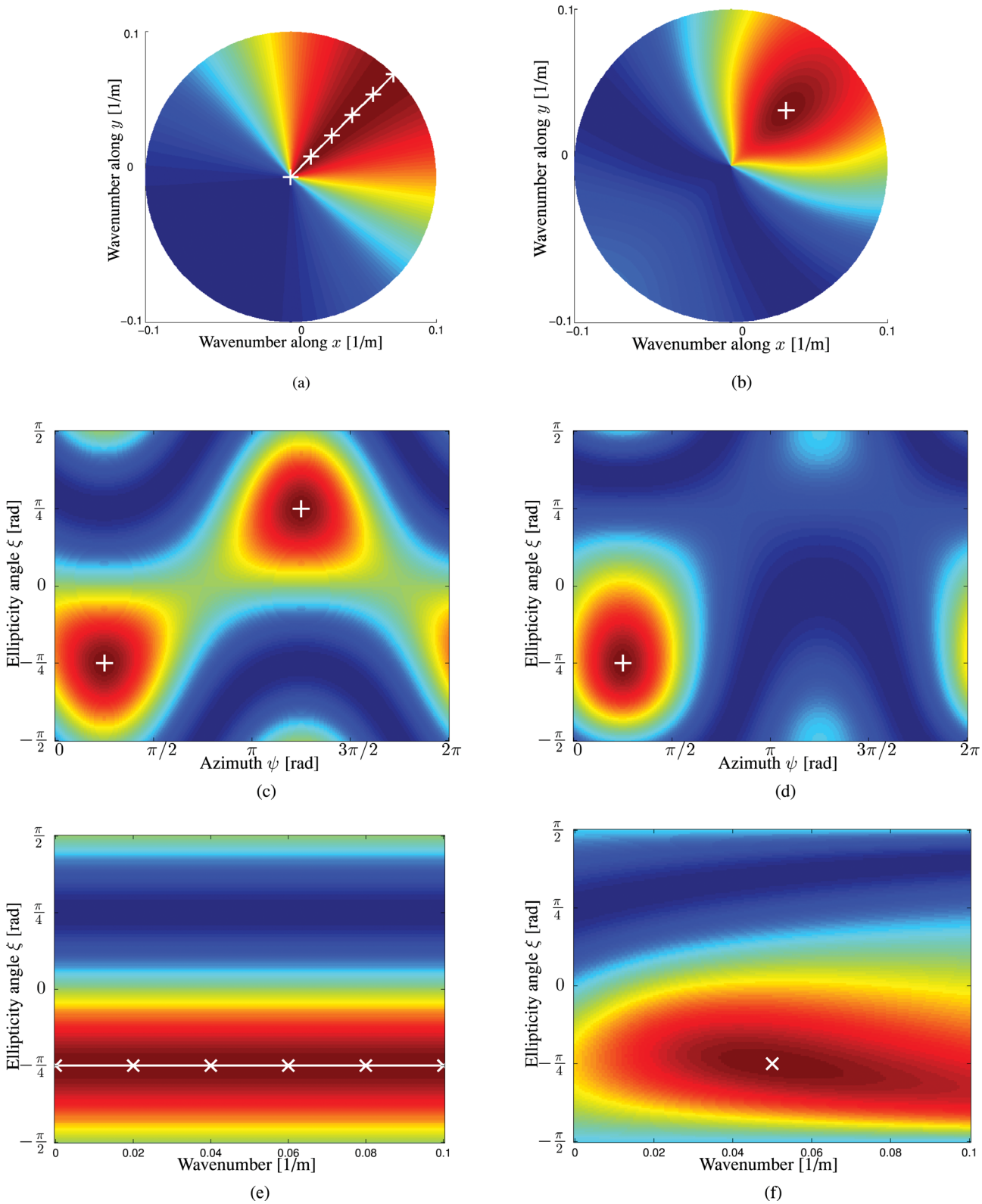

Figure 3. LLFs of observations from a single sensor of a single Rayleigh wave as a function of wavenumber κ, azimuth ψ and ellipticity angle ξ. Comparison of analysis of sole translational components (left-hand panel) and joint translational and rotational components (right-hand panel). Large LL values are shown with colours towards red and low LL values with colours towards blue. White crosses and lines mark the maxima point. (a) Slice of the LLF for $\xi = -\pi/4$ (retrograde motion). (b) Slice of the LLF for $\xi = -\pi/4$. The LLF exhibit a single maxima. (c) Slice of the LLF as a function of ξ and ψ for $\kappa = 0.05$. The likelihood is maximized for opposite direction of propagation with different sense of rotation (prograde ($\pi/2$) or retrograde ($-\pi/2$)). (d) Slice of the LLF as a function of ξ and ψ for $\kappa = 0.05$. Direction of propagation and sense of rotation are pinpointed correctly. (e) Slice of the LLF as a function of κ and ξ for $\psi = \pi/4$. The function is constant for different wavenumbers, because any wavenumber value fits the data equally well. (f) Slice of the LLF as a function of κ and ξ for $\psi = \pi/4$. The wavenumber can be correctly estimated using a six components sensor.

point is seen in correspondence of the true wavefield parameters. Indeed a single six components sensor allows the determination of velocity of propagation, direction of propagation and Rayleigh wave ellipticity without ambiguity.

From the previous pictures we can empirically confirm the theoretical findings about model identifiability of Section 3 and that, at least under the good conditions of high SNR, the joint processing of translational motions and rotational motions allows to estimate all the wavefield parameters correctly. The broadness of the main peak of the LF suggests that the κ remains difficult to estimate accurately with a single six components sensor. This latter aspect is quantified by the CRB analysis in Section 5.4.

5.3 Example likelihood functions for array of sensors

We now compare the shape of LLFs obtained from array of three components sensors and six components sensors.

We consider an array of five sensors arranged on a circle of radius 20 m as shown in Fig. 4. The same choice of wavefield parameters and SNR of Section 5.2 is used in this section.

In Fig. 5, the LLFs of observations of a single Love wave are shown. It is shown that the local maxima (sidelobes) of the LLF are smaller in the six components case than in the three components case.

In Fig. 6, different slices of the LLFs of observations of a single Rayleigh wave are shown. In this example, the reduction of the local maxima is somewhat limited. The largest improvement is seen in comparing Fig. 6(c) with Fig. 6(d).

By comparing the LLFs in this section with the corresponding LLFs of Section 5.2, we see that using the five sensors array the wavenumber and the azimuth are more easily determined, as witnessed by the peakiness of the LLFs in the two different setups. The reason is that estimation from an array of sensors relies on the very important information extracted from the spatial sampling of the signal. This aspect is quantified in Section 5.4.

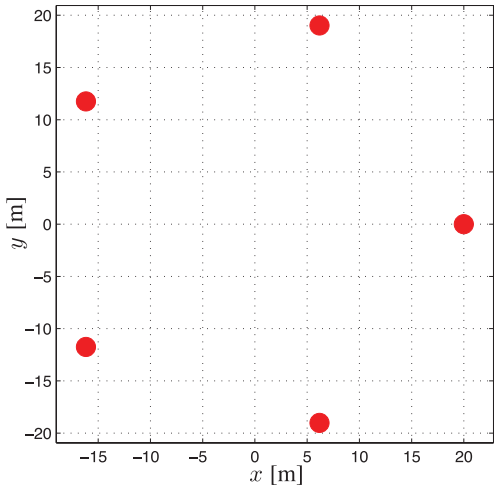

Figure 4. The layout of the five sensors array used in the numerical examples.

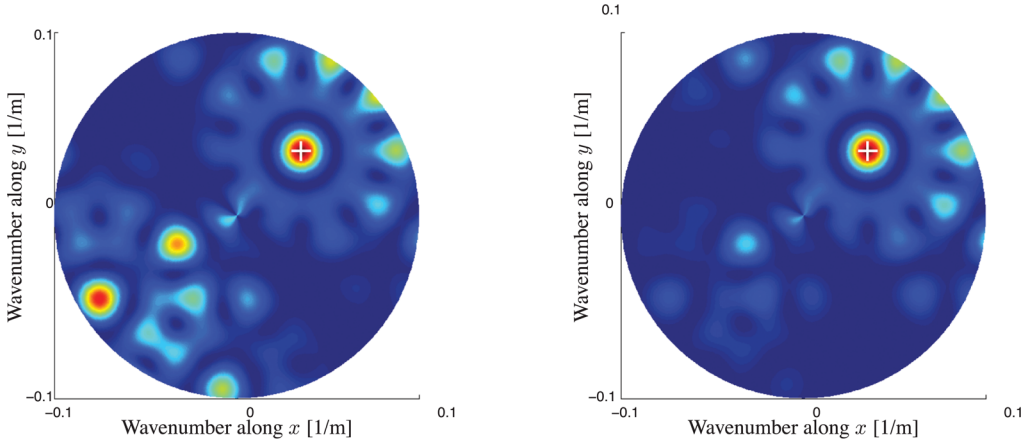

Figure 5. LLFs of observations from a five sensors array of a single Love wave as a function of wavenumber κ and azimuth ψ. Comparison of analysis of sole translational components (left-hand panel) and joint translational and rotational components (right-hand panel). Large LL values are shown with colours towards red and low LL values with colours towards blue. White crosses mark the maxima point. (a) LLF obtained from translational components only. (b) LLF obtained from translational and rotational components jointly.

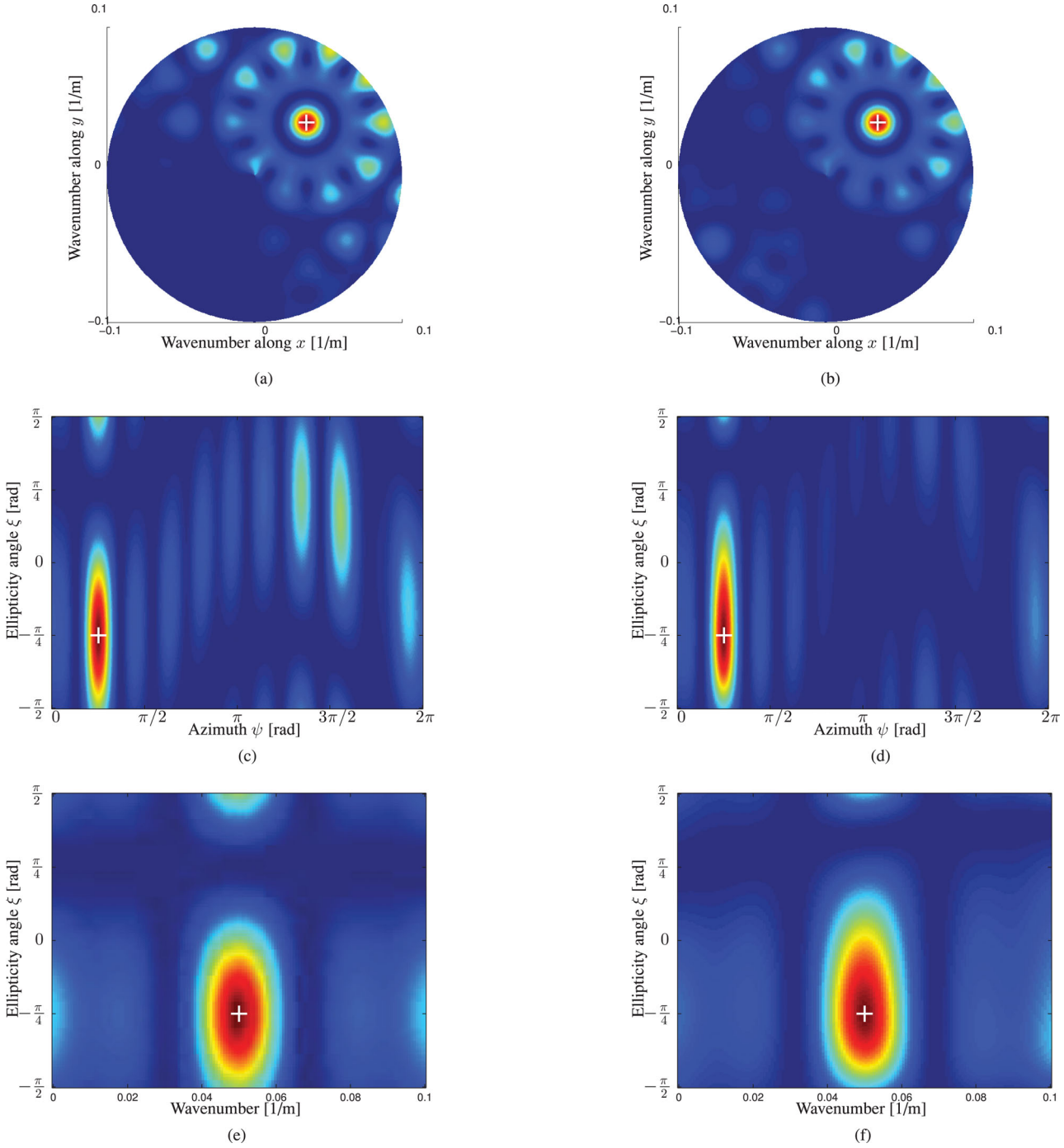

Figure 6. LLFs of observations from a five sensor array of a single Rayleigh wave as a function of wavenumber κ, azimuth ψ and ellipticity angle ξ. Comparison of analysis of sole translational components (left-hand panel) and joint translational and rotational components (right-hand panel). Large LL values are shown with colours towards red and low LL values with colours towards blue. White crosses mark the maxima point. (a) Slice of the LLF as a function for $\xi = -\pi/4$. (b) Slice of the LLF for $\xi = -\pi/4$. (c) Slice of the LLF as a function of ξ and ψ for $\kappa = 0.05$. (d) Slice of the LLF as a function of ξ and ψ for $\kappa = 0.05$. (e) Slice of the LLF as a function of κ and ξ for $\psi = \pi/4$. (f) Slice of the LLF as a function of κ and ξ for $\psi = \pi/4$.

5.4 Cramér-Rao bound analysis

We are interested in comparing the MSEE obtained processing three components and six components with the theoretical bounds given by the CRB derived in Section 3.4.

Fig. 7 portrays the MSEE obtained by means of Monte-Carlo simulations with different processing settings as a function of SNR. The five sensors array depicted in Fig. 4 is considered, with three components sensors and with six components sensors. We also consider the performances of a single six components sensor. The wavefield parameters are the same used in the numerical examples of the previous

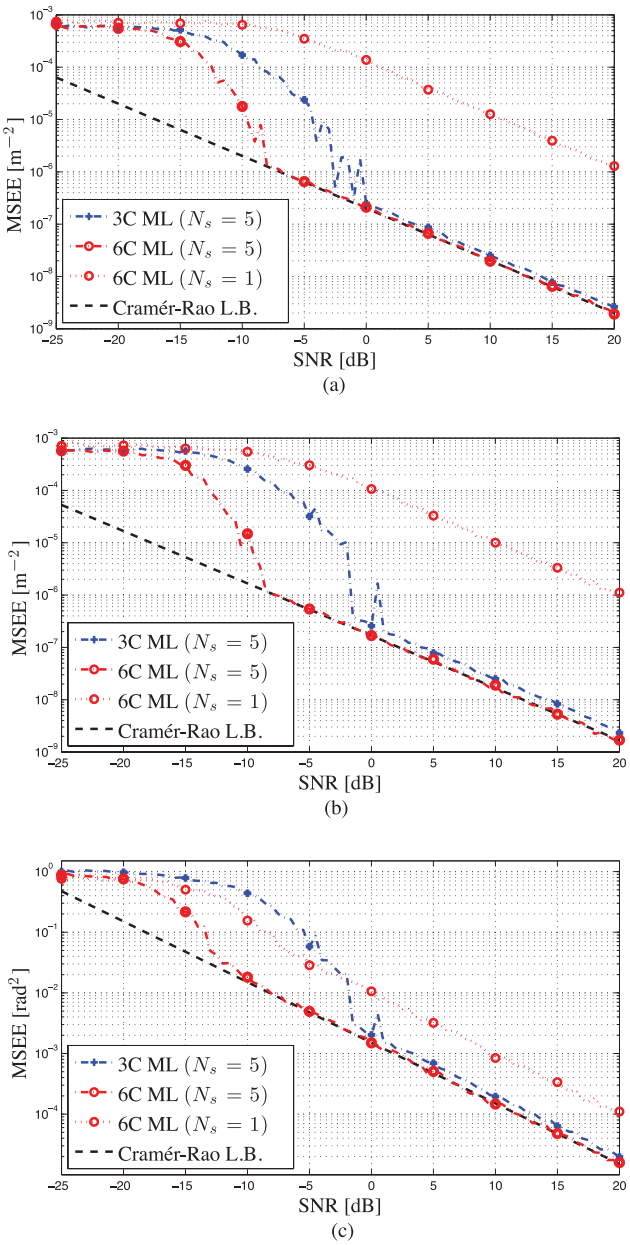

Figure 7. Comparison of the MSEE from different processing setups with the CRB at different SNR. The processing of three components (3C) translational sensors is compared with six components (6C) translational and rotational sensors. Different number of sensors N_s is also compared. (a) Love wavenumber MSEE. (b) Rayleigh wavenumber MSEE. (c) Rayleigh ellipticity angle MSEE.

section and are unknown to the algorithm. Both σ_t^2 and σ_r^2 are unknown to the algorithm and estimated. The true values σ_t^2 and σ_r^2 are chosen as explained in the introduction of this section in order to have comparable SNR on both sensor types.

In Fig. 7(a) the estimation of Love wave wavenumber is analysed. At very low SNR, where the noise dominates, the estimate is substantially random. The MSEE saturates for decreasing SNR since the wavenumber estimate is constrained by the algorithm implementation to belong to a finite interval. As the SNR increases, the ML method using six components always exhibits the smaller MSEE. In the threshold region, approximately in the interval $(-16, -3)$ dB, the performance gain due to the reduction of the outliers of the six components array over the three components array is substantial. This aspect was discussed in Section 3.5. For sufficiently large SNR, the ML method using six components achieves the CRB. Even for high SNR, the three components array does not achieve the CRB as it disregards the rotational measurements.

It is worth noting that the performance gap observed when comparing the three components array with the six components array in the asymptotic region is strongly dependent on the choice of σ_t^2 and σ_r^2. For very large σ_r^2, the rotational measurements become uninformative and the performance gap will narrows to zero. On the other hand, for very large σ_t^2, the translational measurement become uninformative and therefore the three components array will exhibit poor performance while the six components will still provide meaningful estimates.

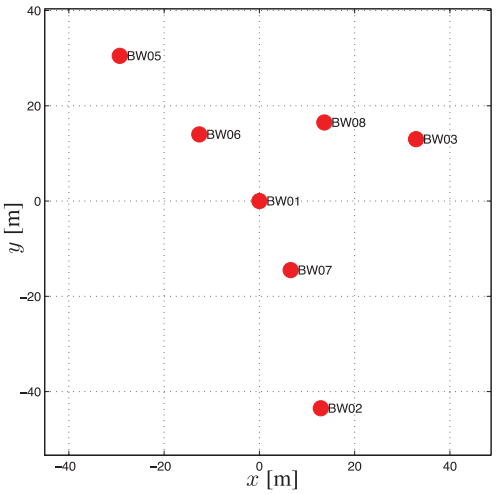

Figure 8. Layout of the array of the Agfa data set. In the central location, at $(x, y) = (0, 0)$, a translational seismometer is colocated with a rotational sensors. The array is centred in 48.108589°N 11.582967°E.

The performance gap between single sensor and any of the two five sensors arrays is considerably large. In order to achieve with a single six components sensor the same MSEE achieved with an array of sensors it is necessary to increase the SNR of several decibels higher. This gap is explained by the fact that the single sensor only relies on amplitude information and disregards the phase information relative to wave propagation. This is also quantified analytically by the expression of the CRBs in Section 3.

In Fig. 7(b), the estimation of Rayleigh wave wavenumber is analysed. In this scenario the considerations are similar to the previous case.

In Fig. 7(c), the estimation of Rayleigh wave ellipticity angle is analysed. In this scenario we observe how the single six component sensor exhibits smaller MSEE than the three components array over a certain SNR range.

Concerning the Rayleigh ellipticity angle estimation, the performance gap is smaller than the previous case. Indeed the CRB on Rayleigh wave ellipticity for a translational array does not rely on phase information, *cf.* (30).

Fig. 7 also shows that our implementation of the ML estimator achieves, for sufficiently large SNR, the CRB in all the considered cases.

5.5 Analysis of the Agfa data set

The Agfa data set consist of recordings of an explosion from building demolition in southern Germany (Wassermann *et al.* 2009). The seismic motion is recorded by an array of seven translational sensors and one rotational sensor. The array layout is depicted in Fig. 8. The rotational sensor is collocated with a translational sensor at the central location labelled 'BW01'. The translational velocimeters are of different make and model as explained in Wassermann *et al.* (2009), the rotational sensor is a eentec R1 (Bernauer *et al.* 2012).

The portion of interest of the recording is only 10 s long and it is split in 0.75 s window which are processed independently with a 50 per cent overlap.

We apply the considered ML method and process the signals recorded by the seven translational sensors modelling the presence of a single Rayleigh wave. The retrieved dispersion curve is depicted in Fig. 9(a). Estimated parameters (wavenumber and ellipticity angle) are shown with a scale of grays, with darker colors corresponding to a value being more often estimated. The red dashed lines represent a manual pick of upper and lower boundaries of the dispersion curve as identified by visual inspection. The red dots depict the estimated dispersion curve starting from such manual selection obtained as the median of the values in the selection. The blue lines represent constant velocity lines. Empirical array resolution limits according to Asten & Henstridge (1984) are depicted with thin dashed black lines. The stripes visible in the figure are due to the fact that the wavenumber estimates within the same time window and at neighbouring frequencies are strongly correlated. In other words, the maximum of the LF changes only slightly when the frequency ω is changed slightly.

The ellipticity angle is shown in Fig. 9(b). Rayleigh particle motion is retrograde, that is, $\xi \in (-\pi/2, 0)$, for frequencies above 4 Hz. Below this frequency the wave appears to be close to horizontally polarized ($\xi = \pm\pi/2$). It should be also considered that at low frequencies the wavenumber estimates are below the conventional resolution limit.

For the single sensor setting, we process the recording of the colocated translational sensor and rotational sensor at position BW01. The wavenumber estimates are shown in Fig. 9(c). From this picture it is possible to recognize a general increase in the values of the estimated wavenumbers. Compared to the results obtained from the array (Fig. 9a), it is possible to see a shift of the estimated wavenumbers towards lower values (faster velocities). One possible explanation is that the sensor are, due to physical constraints, not exactly colocated while the algorithm assume they are both located at the same position. Moreover, the estimation of the wavenumber from single station is affected by the possible presence of higher modes of propagation, as suggested in Kurrle *et al.* (2010). In the single sensor setting, the dispersion curve does not appear to be reliable below 4 Hz and manual selection is not performed.

Estimates of the ellipticity angle are shown in Fig. 9(d) and are in good agreement with the results obtained from the array processing of Fig. 9(b). As expected from the CRB analysis, the scatter of the estimates is to some extent larger in the single sensor setting than in the array setting.

The same recording is processed modelling the presence of a single Love wave. In Fig. 10(a), wavenumber estimates obtained from the processing of the seven translational sensors are shown. In Fig. 10(b), wavenumber estimates obtained from the processing of the sensors colocated at BW01 are shown. Similarly to the case for Rayleigh wave, a shift towards faster velocities is observed.

Love wave wavenumber estimates are more scattered than Rayleigh estimates and the dispersion curve is more difficult to observe. An explanation could be that the Love waves are not as strong because of the nature of the source. Indeed an explosion excites mostly compressional waves and only to a lesser extent shear waves. The branching of the dispersion curve that can be observed below 4 Hz in Fig. 10(a) could also be explained by the little energy of the Love wave.

5.6 Analysis of the TAIGER data set

The TAIGER data set includes recordings of two explosions in northeastern Taiwan (Lin *et al.* 2009). Recordings from an array of eleven accelerometers and five rotational sensors are used. The array layout is depicted in Fig. 11(a). The rotational sensors are colocated with the accelerometers in the five inner locations. In this work, we use recording from the explosion N3P, as named in the referenced paper.

The total duration is around 7 s, the recording is subdivided in 50 per cent overlapping windows of 1 s. The only preprocessing step we purse is to convert the velocity recordings from the rotational sensors to acceleration (rad s^{-2}).

Fig. 11(b) shows the wavenumber estimates obtained processing the signals from the translational sensors. It is difficult to determine the wavenumber change with frequency. Associated ellipticity angle estimates are very scattered and not shown.

In Fig. 11(c) all the available sensors, both translational and rotational are processed jointly. Here the dispersion curve is well identified and the improvement on the previous picture is significant. At last, Fig. 11(d) shows the estimated ellipticity angle obtained from the processing

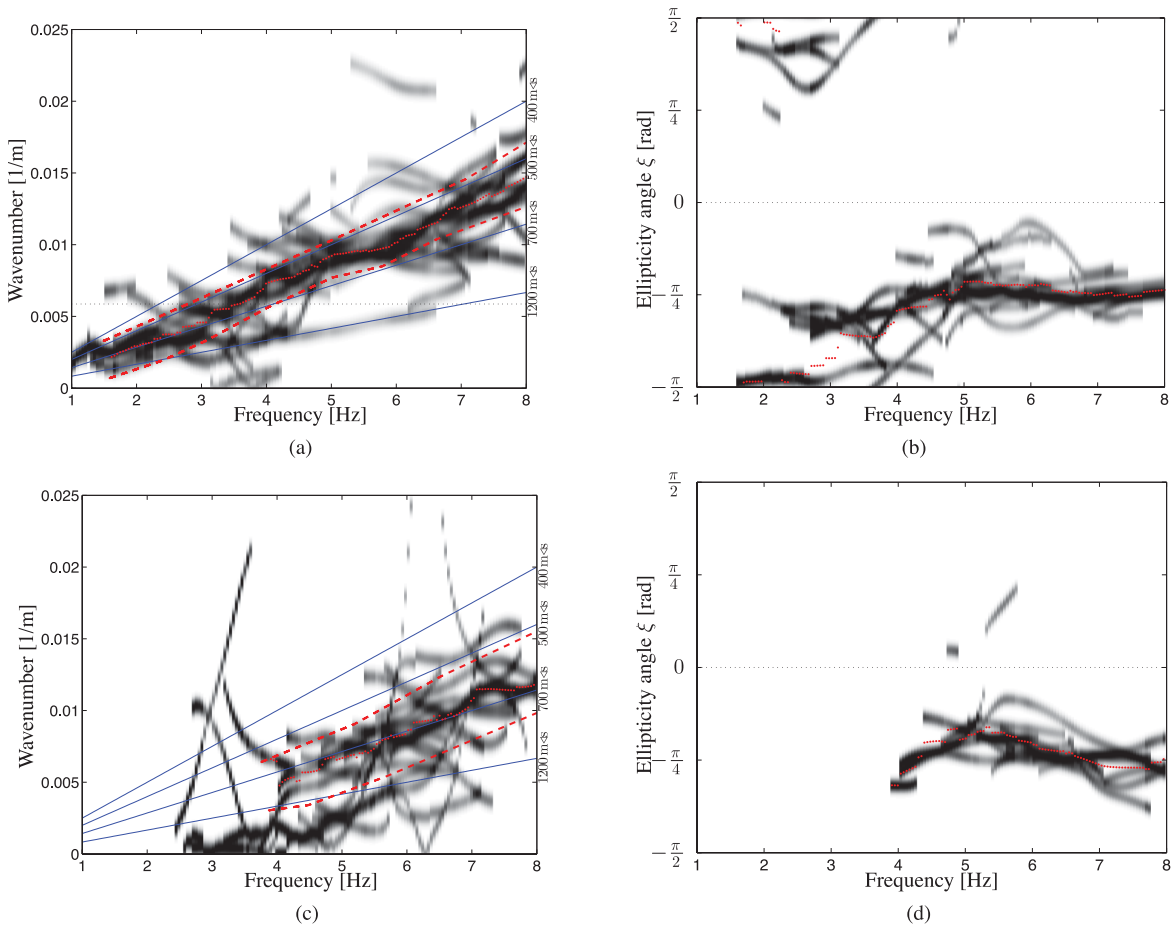

Figure 9. Analysis of Rayleigh waves for the Agfa data set. On the top processing from seven translational sensors, on the bottom from a single six components (translational and rotational) sensor. (a) Rayleigh wavenumber estimated using the array of translational sensors. (b) Rayleigh ellipticity angle estimated using the array of translational sensors. (c) Rayleigh wavenumber estimated using a single six components sensor. (d) Rayleigh ellipticity angle estimated using a single six components sensor.

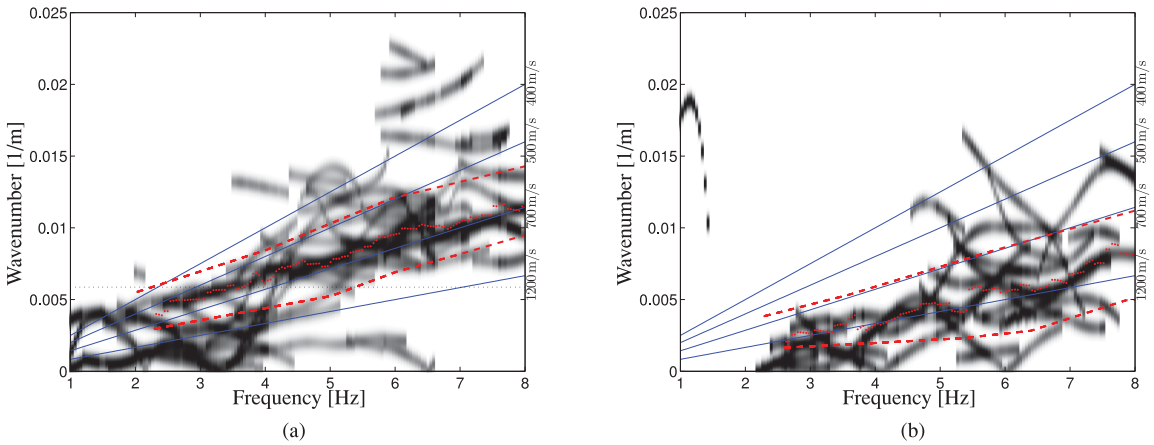

Figure 10. Analysis of Love waves for the Agfa data set. On the left processing from seven translational sensors, on the right from a single six components (translational and rotational) sensor. (a) Love wavenumber estimated using the array of translational sensors. (b) Love wavenumber estimated using a single six components sensor.

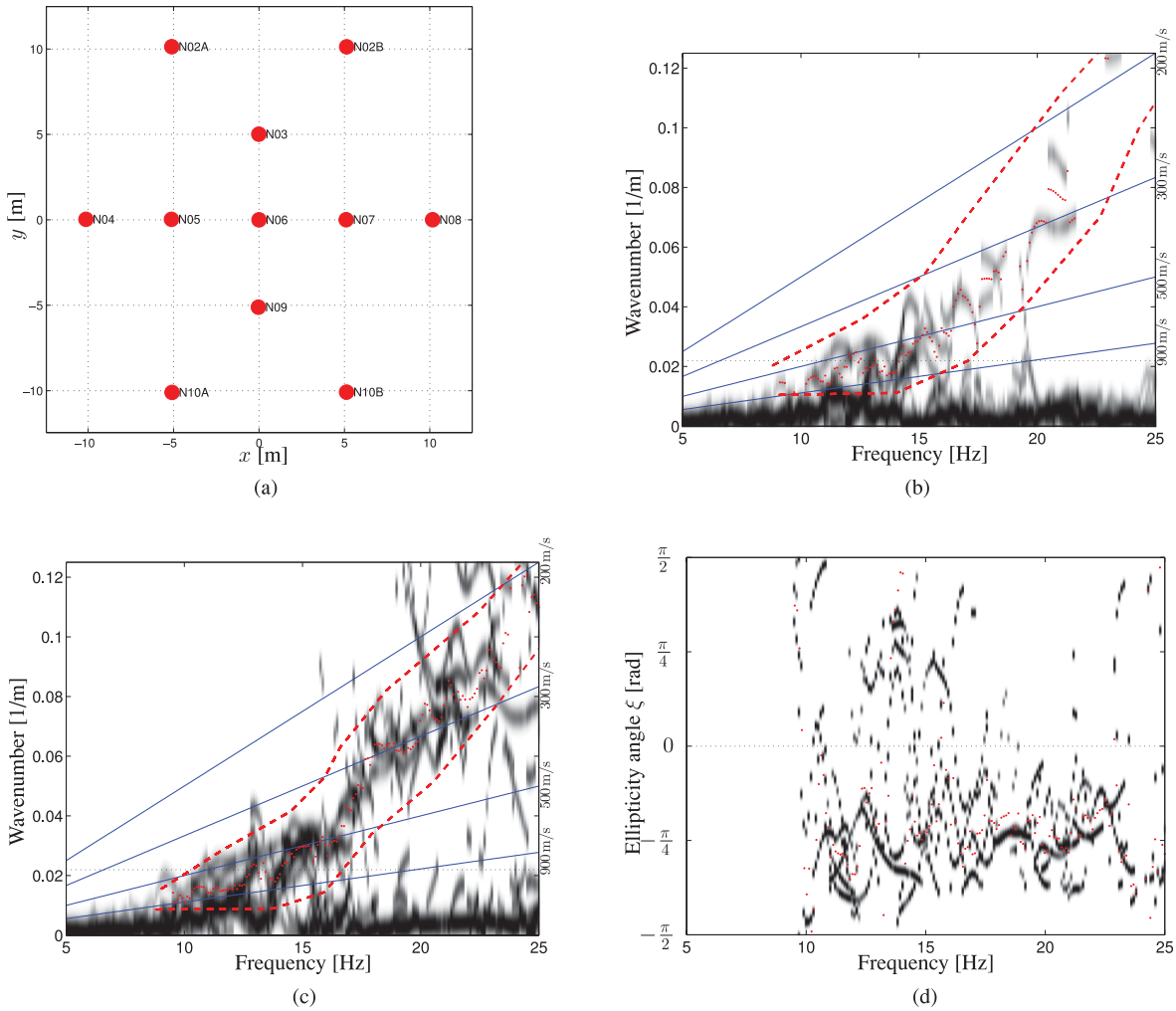

Figure 11. Analysis of Rayleigh waves for the TAIGER data set. (a) Array layout for the TAIGER data set. Five rotational sensors are colocated with translational sensors in the inner five locations of the array. The array is centred at 24.5792222°N 121.4818722°E. (b) Rayleigh wavenumber from processing of translational sensors. (c) Rayleigh wavenumber from joint processing of translational and rotational sensors. (d) Rayleigh ellipticity angle from joint processing of translational and rotational sensors.

of all the sensors. Despite the scatter it is possible to identify a retrograde particle motion at frequencies above 10 Hz. Below this frequency the wave is substantially horizontally polarized.

The estimation of the wavenumber and ellipticity angle is significantly improved by the joint processing of translational and rotational sensors over the processing of the sole translational sensors. We observe that the array is rather small, 20 m in diameter, and this might be a limiting factor in the estimation of the wavenumber of seismic waves with wavelengths between 10 and 50 m. We speculate that in this setting the amplitude information provided by the rotational sensors is particularly important.

Comparing the estimated wavenumber at different time windows (not shown) it is possible to see a tendency of a shift of wavenumbers towards smaller values, that is, slower velocity with increasing time. This shift could be explained by the nonlinear behaviours induced by the large strains. This observation however remains speculative, due to missing independent observation such as pore-pressure build-up in the soils.

6 CONCLUSIONS

In this paper, we study different aspects of the processing of translational motions and rotational motions for surface waves. Using tools from statistics, we investigate the contribution of the different measurements types to the accuracy of wavefield parameters estimation. Advantages and limitations of single and array of sensors are outlined quantitatively with respect to identifiability of the statistical models and lower bounds on the estimation accuracy. These findings are also useful for experiment design and to compare estimation algorithms with an implementation-independent benchmark. We show several numerical examples clarifying the theoretical aspects for both single sensor and array settings.

A method for ML estimation of wavefield parameters is considered. The method extends a previous work of the authors and accounts for all the measurements and all the wavefield parameters within a single statistical model. In this context we show the estimation of wave parameters of both Love waves and Rayleigh waves from arrays of sensors and single sensors using jointly translational and rotational recordings. In addition, the method accounts for different noise level on each sensor.

Firstly, using Monte Carlo simulations we show that our method achieves, for sufficiently large SNR, the theoretical lower bounds on estimation accuracy. We also show that the performance loss in wavenumber estimation is significant when using a single six components sensor instead of a five sensors array. This is due to the lack of information extracted from spatial sampling of the signal and is also explained by our theoretical findings.

Secondly, we demonstrate, on real recordings, the applicability of the proposed method for the estimation of Love wave and Rayleigh wave parameters for both single sensor and array settings. In the Agfa data set, we retrieve Love and Rayleigh dispersions curves from single six component sensor and compare with the dispersion curve retrieved from an array of translational sensors. Using a single six component sensor, we observe a shift of the estimated wavenumbers towards faster velocities when compared to the array retrieved dispersion. For the same data set we also retrieve Rayleigh wave ellipticity angle from the single sensor and find agreement with the same quantity estimated from the array of sensors. Concerning the TAIGER data set, we compare Rayleigh wave dispersion curve obtained from a three component (translational) array and an array of mixed three- and six-components sensors. We find that the joint analysis of translational and rotational sensors greatly improve the retrieved dispersion curve.

It is expected that the interest of the seismological community in this area to grow further in the coming years. As sensor technology will develop further improving the quality and the availability of rotational measurements a wide range of applications will be possible.

ACKNOWLEDGEMENTS

We wish to thank the authors of Wassermann *et al.* (2009) and Lin *et al.* (2009) for making the recordings of the Agfa and the TAIGER data sets available. The authors also wish to thank Dr. Edwards for the careful reading of the manuscript. The authors also would like to thank the anonymous reviewers for their comments and helping to improve the manuscript.

This work is supported in part by the Swiss Commission for Technology and Innovation under project 9260.1 PFIW-IW and with funds of the Swiss Seismological Service.

REFERENCES

Aki, K. & Richards, P.G., 2002. *Quantitative Seismology,* 2nd edn, University Science Books, Sausalito, CA.

Asten, M.W. & Henstridge, J.D., 1984. Array estimators and the use of microseisms for reconnaissance of sedimentary basins, *Geophysics,* **49**(11), 1828–1837.

Athley, F., 2008. Threshold region performance of maximum likelihood direction of arrival estimators, *IEEE Trans. Signal Process.,* **56**(8), 1359–1373.

Bernauer, F., Wassermann, J. & Igel, H., 2012. Rotational sensors: a comparison of different sensor types, *J. Seism.,* **16**(4), 595–602.

Bonnefoy-Claudet, S., Cornou, C., Bard, P.-Y., Cotton, F., Moczo, P., Kristek, J. & Fäh, D., 2006. H/V ratio: a tool for site effects evaluation. Results from 1-D noise simulations, *Geophys. J. Int.,* **167**(2), 827–837.

Capon, J., 1969. High-resolution frequency-wavenumber spectrum analysis, *Proc. IEEE,* **57**(8), 1408–1418.

Cox, H. & Lai, H., 2007. Performance of line arrays of vector and higher order sensors, in *Conference Record of the 41st Asilomar Conference on Signals, Systems, and Computers,* pp. 1231–1236, Pacific Grove, CA.

Cramér, H., 1946. *Mathematical Methods of Statistics,* Princeton Univ. Press, Princeton, NJ.

Fäh, D., Kind, F. & Giardini, D., 2003. Inversion of local S-wave velocity structures from average H/V ratios, and their use for the estimation of site-effects, *J. Seism.,* **7,** 449–467.

Fäh, D., Stamm, G. & Havenith, H.-B., 2008. Analysis of three-component ambient vibration array measurements, *Geophys. J. Int.,* **172**(1), 199–213.

Ferreira, A. M.G. & Igel, H., 2009. Rotational motions of seismic surface waves in a laterally heterogeneous earth, *Bull. seism. Soc. Am.,* **99**(2B), 1429–1436.

Fichtner, A. & Igel, H., 2009. Sensitivity densities for rotational ground-motion measurements, *Bull. seism. Soc. Am.,* **99**(2B), 1302–1314.

Fisher, R.A., 1922. On the mathematical foundations of theoretical statistics, *Phil. Trans. R. Soc. Lond., A.,* **222,** 309–368.

Hawkes, M. & Nehorai, A., 1998. Acoustic vector-sensor beamforming and Capon direction estimation, *IEEE Trans. Signal Process.,* **46**(9), 2291–2304.

Hobiger, M., Bard, P., Cornou, C. & Le Bihan, N., 2009. Single station determination of Rayleigh wave ellipticity by using the random decrement technique (RayDec), *Geophys. Res. Lett.,* **36,** L14303, doi:10.1029/2009GL038863.

Horn, R.A. & Johnson, C.R., 1990. *Matrix Analysis,* Cambridge Univ. Press, Cambridge, UK.

Igel, H., Schreiber, U., Flaws, A., Schuberth, B., Velikoseltsev, A. & Cochard, A., 2005. Rotational motions induced by the M8.1 Tokachi-oki earthquake, September 25, 2003, *Geophys. Res. Lett.,* **32,** L08309, doi:10.1029/2004GL022336.

Igel, H., Brokesova, J., Evans, J. & Zembaty, Z., 2012. Preface to the special issue on "Advances in rotational seismology: instrumentation, theory, observations, and engineering", *J. Seism.,* **16**(4), 571–572.

Kay, S.M., 1993. *Fundamentals of Statistical Signal Processing: Estimation Theory,* Prentice Hall, Upper Saddle River, NJ.

Kschischang, F.R., Frey, B.J. & Loeliger, H.-A., 2001. Factor graphs and the sum-product algorithm, *IEEE Trans. Inf. Theory,* **47**(2), 498–519.

Kurrle, D., Igel, H., Ferreira, A.M., Wassermann, J. & Schreiber, U., 2010. Can we estimate local Love wave dispersion properties from collocated amplitude measurements of translations and rotations?, *Geophys. Res. Lett.,* **37,** L04307, doi:10.1029/2009GL042215.

Lacoss, R., Kelly, E. & Toksöz, M., 1969. Estimation of seismic noise structure using arrays, *Geophysics,* **34**(1), 21–38.

Lee, W. H.K., Çelebi, M., Todorovska, M.I. & Igel, H., 2009. Introduction to the special issue on rotational seismology and engineering applications, *Bull. seism. Soc. Am.,* **99**(2B), 945–957.

Lee, W. H.K., Evans, J.R., Huang, B.-S., Hutt, C.R., Lin, C.-J., Liu, C.-C. & Nigbor, R.L., 2012. Measuring rotational ground motions in seismological practice, in *New Manual of Seismological Observatory Practice 2,* pp. 1–27, ed. Bormann, P., Deutsches GeoForschungsZentrum, Potsdam.

Leugoud, R. & Kharlamov, A., 2012. Second generation of a rotational electrochemical seismometer using magnetohydrodynamic technology, *J. Seism.,* **16**(4), 587–593.

Lin, C.-J., Liu, C.-C. & Lee, W. H.K., 2009. Recording rotational and translational ground motions of two TAIGER explosions in northeastern taiwan on 4 March 2008, *Bull. seism. Soc. Am.,* **99**(2b), 1237–1250.

Loeliger, H.-A., 2004. An introduction to factor graphs, *IEEE Signal Process. Mag.,* **21**(1), 28–41.

Loeliger, H.-A., Dauwels, J., Hu, J., Korl, S., Ping, L. & Kschischang, F.R., 2007. The factor graph approach to model-based signal processing, *Proc. IEEE,* **95**(6), 1295–1322.

Maranò, S., Reller, C., Fäh, D. & Loeliger, H.-A., 2011. Seismic waves estimation and wave field decomposition with factor graphs, in *Proceedings of the IEEE International Conference Acoustics, Speech, and Signal Processing,* pp. 2748–2751, Prague, Czech Republic.

Maranò, S., Reller, C., Loeliger, H.-A. & Fäh, D., 2012. Seismic waves estimation and wavefield decomposition: application to ambient vibrations, *Geophys. J. Int.,* **191**(1), 175–188.

Niazi, M., 1986. Inferred displacements, velocities and rotations of a long rigid foundation located at El Centro differential array site during the 1979 Imperial Valley, California, earthquake, *Earthq Eng. Struct. Dynam.,* **14**(4), 531–542.

Nigbor, R., 1994. Six-degree-of-freedom ground-motion measurement, *Bull. seism. Soc. Am.,* **84**(5), 1665–1669.

Nigbor, R., Evans, J. & Hutt, C., 2009. Laboratory and field testing of commercial rotational seismometers, *Bull. seism. Soc. Am.,* **99,** 1215–1227.

Okada, H., 1997. *The Microtremor Survey Method,* Society of Exploration Geophysicists, Tulsa, OK.

Oliveira, C. & Bolt, B., 1989. Rotational components of surface strong ground motion, *Earthq. Eng. Struct. Dynam.,* **18**(4), 517–526.

Poggi, V. & Fäh, D., 2010. Estimating Rayleigh wave particle motion from three-component array analysis of ambient vibrations, *Geophys. J. Int.,* **180**(1), 251–267.

Poggi, V., Fäh, D., Burjanek, J. & Giardini, D., 2012. The use of Rayleigh-wave ellipticity for site-specific hazard assessment and microzonation: application to the city of Lucerne, Switzerland, *Geophys. J. Int.,* **188**(3), 1154–1172.

Rao, C.R., 1945. Information and accuracy attainable in the estimation of statistical parameters, *Bull. Calcutta Math. Soc.,* **37,** 81–91.

Reller, C., Loeliger, H.-A. & Maranò, S., 2011. Multi-sensor estimation and detection of phase-locked sinusoids, in *Proceedings of the IEEE International Conference Acoustics, Speech, and Signal Processing,* pp. 3872–3875, Prague, Czech Republic.

Rothenberg, T.J., 1971. Identification in parametric models, *Econometrica,* **39**(3), 577–591.

Schreiber, K., Hautmann, J., Velikoseltsev, A., Wassermann, J., Igel, H., Otero, J., Vernon, F. & Wells, J., 2009. Ring laser measurements of ground rotations for seismology, *Bull. seism. Soc. Am.,* **99**(2B), 1190–1198.

Shen, Y. & Win, M.Z., 2010. On the accuracy of localization systems using wideband antenna arrays, *IEEE Trans. Commun.,* **58**(1), 270–280.

Spudich, P., Steck, L.K., Hellweg, M., Fletcher, J.B. & Baker, L.M., 1995. Transient stresses at Parkfield, California, produced by the M7.4 Landers earthquake of June 28, 1992: observations from the UPSAR dense seismograph array, *J. geophys. Res.,* **100,** 675–690.

Stoica, P., Moses, R., Friedlander, B. & Söderstrom, T., 1989. Maximum likelihood estimation of the parameters of multiple sinusoids from noisy measurements, *IEEE Trans. Acoust., Speech, Signal Process.,* **37**(3), 378–392.

Suryanto, W. *et al.*, 2006. First comparison of array-derived rotational ground motions with direct ring laser measurements, *Bull. seism. Soc. Am.,* **96**(6), 2059–2071.

Tokimatsu, K., 1997. Geotechnical site characterization using surface waves, in *Proceedings of the 1st International Conference Earthquake Geotechnical Engineering,* pp. 1333–1368, Balkema.

Van Trees, H.L., 2001. *Detection, Estimation, and Modulation Theory: Part I,* John Wiley & Sons, Inc., New York.

Wassermann, J., Lehndorfer, S. & Igel, H., 2009. Performance test of a commercial rotational motions sensor, *Bull. seism. Soc. Am.,* **99**(2B), 1449–1456.

APPENDIX A: DERIVATION OF FISHER INFORMATION MATRICES

The FIM can be derived using (17) and (12) together with one of the wave model presented in Section 2. Six distinct FIMs are presented in this section, corresponding to the wave type Love or Rayleigh and the measurement type translational, rotational, or both.

The noise variances $\{\sigma_\ell\}_{\ell=1,\ldots,L}$ are in general also unknown parameters of the statistical model. However, for the purposes of this discussion, we assume the noise variances to be known and derive the FIM only for the wavefield parameters $\boldsymbol{\theta}$. This choice is supported by

the fact that

$$\mathcal{I}_{\theta_i,\sigma_\ell^2} = \mathsf{E}\left\{-\frac{\partial^2 \ln p_{\boldsymbol{Y}}(\boldsymbol{y}|\boldsymbol{\theta},\sigma_1^2,\ldots,\sigma_L^2)}{\partial\theta_i\partial\sigma_\ell^2}\right\} = 0\,,$$

implying that the wavefield parameters and the noise variances are decoupled. Thus, all the derivation to follow can accommodate for the case of unknown noise variances $\{\sigma_\ell\}_{\ell=1,\ldots,L}$ with trivial modifications.

With the measurement model presented in (12) and assuming the variance on channel ℓ to be known and equal to σ_ℓ^2, then (17) reduces to a simpler expression (Kay 1993). The element in position i,j of $\boldsymbol{\mathcal{I}}$ is obtained as

$$[\boldsymbol{\mathcal{I}}(\boldsymbol{\theta})]_{i,j} = \sum_{\ell=1}^{L}\frac{1}{\sigma_\ell^2}\sum_{k=1}^{K}\frac{\partial u_k^{(\ell)}}{\partial\theta_i}\frac{\partial u_k^{(\ell)}}{\partial\theta_j}\,. \tag{A1}$$

We further assume that the noise variances are equal to σ_{t}^2 for translational measurement and are equal to σ_{r}^2 for rotational measurements.

In the derivation of the FIMs the two following approximations are used (see Kay 1993, example 3.14 or Stoica *et al.* 1989)

$$\sum_{k=1}^{K}\cos^2(\omega k+\beta) \approx \frac{K}{2} \tag{A2}$$

$$\sum_{k=1}^{K}\sin^2(\omega k+\beta) \approx \frac{K}{2} \tag{A3}$$

$$\sum_{k=1}^{K}\sin(\omega k+\beta)\cos(\omega k+\beta) \approx 0, \tag{A4}$$

which are valid for ω being not near 0 or 1/2 and are exact when $\omega = \frac{2\pi m}{K}$ $m \in \mathbb{Z}$.

According to the model of (23) and (24), a Love wave is parametrized with the vector $\boldsymbol{\theta}^{(\mathrm{L})} = (\alpha, \varphi, \kappa, \psi)^{\mathrm{T}}$, thus the corresponding FIM is $\boldsymbol{\mathcal{I}}(\boldsymbol{\theta}^{(\mathrm{L})}) \in \mathbb{R}^{4\times4}$. From (7) and using (A1) is derived the FIM for the model of a single Love wave and translational measurements, which is

$$\boldsymbol{\mathcal{I}}_{\mathrm{t}}(\boldsymbol{\theta}^{(\mathrm{L})}) = \frac{\alpha^2 K}{2\sigma_{\mathrm{t}}^2}\begin{pmatrix} \frac{N_{\mathrm{s}}}{\alpha^2} & 0 & 0 & 0 \\ 0 & N_{\mathrm{s}} & \sum_{n=1}^{N_{\mathrm{s}}}\frac{\partial\Phi_n}{\partial\kappa} & \sum_{n=1}^{N_{\mathrm{s}}}\frac{\partial\Phi_n}{\partial\psi} \\ 0 & \sum_{n=1}^{N_{\mathrm{s}}}\frac{\partial\Phi_n}{\partial\kappa} & \sum_{n=1}^{N_{\mathrm{s}}}\left(\frac{\partial\Phi_n}{\partial\kappa}\right)^2 & \sum_{n=1}^{N_{\mathrm{s}}}\frac{\partial\Phi_n}{\partial\psi}\frac{\partial\Phi_n}{\partial\kappa} \\ 0 & \sum_{n=1}^{N_{\mathrm{s}}}\frac{\partial\Phi_n}{\partial\psi} & \sum_{n=1}^{N_{\mathrm{s}}}\frac{\partial\Phi_n}{\partial\psi}\frac{\partial\Phi_n}{\partial\kappa} & N_{\mathrm{s}}+\sum_{n=1}^{N_{\mathrm{s}}}\left(\frac{\partial\Phi_n}{\partial\psi}\right)^2 \end{pmatrix}, \tag{A5}$$

with $\Phi_n = -\boldsymbol{\kappa}\cdot\boldsymbol{p}_n + \varphi$.

From (8) and using (A1) is derived the FIM, the model of a single Love wave and rotational measurements, which is

$$\boldsymbol{\mathcal{I}}_{\mathrm{r}}(\boldsymbol{\theta}^{(\mathrm{L})}) = \frac{\alpha^2\kappa^2 K}{8\sigma_{\mathrm{r}}^2}\begin{pmatrix} \frac{N_{\mathrm{s}}}{\alpha^2} & 0 & \frac{N_{\mathrm{s}}}{\alpha\kappa} & 0 \\ 0 & N_{\mathrm{s}} & \sum_{n=1}^{N_{\mathrm{s}}}\frac{\partial\Phi_n}{\partial\kappa} & \sum_{n=1}^{N_{\mathrm{s}}}\frac{\partial\Phi_n}{\partial\psi} \\ \frac{N_{\mathrm{s}}}{\alpha\kappa} & \sum_{n=1}^{N_{\mathrm{s}}}\frac{\partial\Phi_n}{\partial\kappa} & \frac{N_{\mathrm{s}}}{\kappa^2}+\sum_{n=1}^{N_{\mathrm{s}}}\left(\frac{\partial\Phi_n}{\partial\kappa}\right)^2 & \sum_{n=1}^{N_{\mathrm{s}}}\frac{\partial\Phi_n}{\partial\psi}\frac{\partial\Phi_n}{\partial\kappa} \\ 0 & \sum_{n=1}^{N_{\mathrm{s}}}\frac{\partial\Phi_n}{\partial\psi} & \sum_{n=1}^{N_{\mathrm{s}}}\frac{\partial\Phi_n}{\partial\psi}\frac{\partial\Phi_n}{\partial\kappa} & \sum_{n=1}^{N_{\mathrm{s}}}\left(\frac{\partial\Phi_n}{\partial\psi}\right)^2 \end{pmatrix}. \tag{A6}$$

The FIM for the model of a single Love wave using both translational and rotational measurements is obtained adding the two FIM of (A5) and (A6) as in (18)

$$\boldsymbol{\mathcal{I}}(\boldsymbol{\theta}^{(\mathrm{L})}) = \boldsymbol{\mathcal{I}}_{\mathrm{t}}(\boldsymbol{\theta}^{(\mathrm{L})}) + \boldsymbol{\mathcal{I}}_{\mathrm{r}}(\boldsymbol{\theta}^{(\mathrm{L})})\,. \tag{A7}$$

According to (28) and (29) a Rayleigh wave is parametrized with the vector $\boldsymbol{\theta}^{(\mathrm{R})} = (\alpha, \varphi, \kappa, \psi, \xi)^{\mathrm{T}}$, thus the corresponding FIM is $\boldsymbol{\mathcal{I}}(\boldsymbol{\theta}^{(\mathrm{R})}) \in \mathbb{R}^{5\times 5}$. From (9) and using (A1) is derived the FIM for the model of a single Rayleigh wave and translational measurements, which is

$$\boldsymbol{\mathcal{I}}_{\mathrm{t}}(\boldsymbol{\theta}^{(\mathrm{R})}) = \frac{\alpha^2 K}{2\sigma_{\mathrm{t}}^2} \begin{pmatrix} \frac{N_{\mathrm{s}}}{\alpha^2} & 0 & 0 & 0 & 0 \\ 0 & N_{\mathrm{s}} & \sum_{n=1}^{N_{\mathrm{s}}} \frac{\partial \Phi_n}{\partial \kappa} & \sum_{n=1}^{N_{\mathrm{s}}} \frac{\partial \Phi_n}{\partial \psi} & 0 \\ 0 & \sum_{n=1}^{N_{\mathrm{s}}} \frac{\partial \Phi_n}{\partial \kappa} & \sum_{n=1}^{N_{\mathrm{s}}} \left(\frac{\partial \Phi_n}{\partial \kappa}\right)^2 & \sum_{n=1}^{N_{\mathrm{s}}} \left(\frac{\partial \Phi_n}{\partial \kappa}\frac{\partial \Phi_n}{\partial \psi}\right) & 0 \\ 0 & \sum_{n=1}^{N_{\mathrm{s}}} \frac{\partial \Phi_n}{\partial \psi} & \sum_{n=1}^{N_{\mathrm{s}}} \left(\frac{\partial \Phi_n}{\partial \kappa}\frac{\partial \Phi_n}{\partial \psi}\right) & N_{\mathrm{s}} \sin^2 \xi + \sum_{n=1}^{N_{\mathrm{s}}} \left(\frac{\partial \Phi_n}{\partial \psi}\right)^2 & 0 \\ 0 & 0 & 0 & 0 & N_{\mathrm{s}} \end{pmatrix}. \tag{A8}$$

From (10) and using (A1) is derived the FIM for the model of a single Rayleigh wave and rotational measurements, which is

$$\boldsymbol{\mathcal{I}}_{\mathrm{r}}(\boldsymbol{\theta}^{(\mathrm{R})}) = \frac{\alpha^2 \kappa^2 \cos^2 \xi K}{2\sigma_{\mathrm{r}}^2} \begin{pmatrix} \frac{N_{\mathrm{s}}}{\alpha^2} & 0 & \frac{N_{\mathrm{s}}}{\alpha\kappa} & 0 & -\frac{\tan \xi N_{\mathrm{s}}}{\alpha} \\ 0 & N_{\mathrm{s}} & \sum_{n=1}^{N_{\mathrm{s}}} \frac{\partial \Phi_n}{\partial \kappa} & \sum_{n=1}^{N_{\mathrm{s}}} \frac{\partial \Phi_n}{\partial \psi} & 0 \\ \frac{N_{\mathrm{s}}}{\alpha\kappa} & \sum_{n=1}^{N_{\mathrm{s}}} \frac{\partial \Phi_n}{\partial \kappa} & \frac{N_{\mathrm{s}}}{\kappa^2} + \sum_{n=1}^{N_{\mathrm{s}}} \left(\frac{\partial \Phi_n}{\partial \kappa}\right)^2 & \sum_{n=1}^{N_{\mathrm{s}}} \frac{\partial \Phi_n}{\partial \psi}\frac{\partial \Phi_n}{\partial \kappa} & -\frac{\tan \xi N_{\mathrm{s}}}{\kappa} \\ 0 & \sum_{n=1}^{N_{\mathrm{s}}} \frac{\partial \Phi_n}{\partial \psi} & \sum_{n=1}^{N_{\mathrm{s}}} \frac{\partial \Phi_n}{\partial \psi}\frac{\partial \Phi_n}{\partial \kappa} & N_{\mathrm{s}} + \sum_{n=1}^{N_{\mathrm{s}}} \left(\frac{\partial \Phi_n}{\partial \psi}\right)^2 & 0 \\ -\frac{\tan \xi N_{\mathrm{s}}}{\alpha} & 0 & -\frac{\tan \xi N_{\mathrm{s}}}{\kappa} & 0 & \tan^2 \xi N_{\mathrm{s}} \end{pmatrix}. \tag{A9}$$

The FIM for the model of a single Rayleigh wave using both translational and rotational measurements is obtained adding the two FIM of (A8) and (A9) as in (18)

$$\boldsymbol{\mathcal{I}}(\boldsymbol{\theta}^{(\mathrm{R})}) = \boldsymbol{\mathcal{I}}_{\mathrm{t}}(\boldsymbol{\theta}^{(\mathrm{R})}) + \boldsymbol{\mathcal{I}}_{\mathrm{r}}(\boldsymbol{\theta}^{(\mathrm{R})}). \tag{A10}$$